Department of Physics and Astronomy
University of Heidelberg

Pressure and high-voltage calibration of the ALICE Transition Radiation Detector

Bachelor Thesis in Physics
submitted by

Fabio Schlichtmann

born in Heilbronn (Germany)

2018

Abstract:

Within this Bachelor Thesis a method for the pressure and high voltage calibration of the Transition Radiation Detector (TRD) of the ALICE experiment at CERN has been developed. The final signal of the TRD should only depend on the particle and its energy loss in the detector. The detected signal depends on pressure, high voltage settings, gas composition and the geometry of each chamber. All those effects need therefore to be understood in detail. Within a model the gain dependence on pressure was simulated. Moreover I investigated the pressure and high voltage dependence by the usage of data from a krypton calibration run and systematically described those dependencies. After that it is possible to improve the present pressure calibration and find optimal high voltage settings so that the variations of the output signals become minimal.

Kurzfassung:

Im Rahmen dieser Bachelorarbeit wurde die Druck- und Hochspannungskalibrierung des Transition Radiation Detektors (TRD) des ALICE-Experiments am CERN verbessert. Das Signal eines kalibrierten Detektors sollte nur von der Teilchenart und seiner Energie abhängen, jedoch wird es auch von dem Druck, der eingestellten Hochspannung, der Gaszusammensetzung und der Geometrie jeder Kammer beeinflusst. Mithilfe eines Modells wurde die Druckabhängigkeit simuliert. Des Weiteren werde ich insbesondere die Druck- und Hochspannungsabhängigkeit mithilfe von Daten aus dem Krypton-Run untersuchen und systematisch beschreiben. Danach ist es möglich die aktuelle Druckkalibration zu verbessern und optimale Hochspannungswerte zu finden, sodass die Variationen des Ausgangs-Signals minimiert werden.

This Bachelor Thesis has been carried out by Fabio Schlichtmann at the
Physikalisches Institut in Heidelberg
under the supervision of
Prof. Dr. Johanna Stachel

Contents

1 Introduction: Heavy-Ion Physics

The Standard Model of particle physics tells us that our universe consists only of a few elementary particles which can be divided in matter, quarks and leptons, and mediator particles, called bosons [1]. These fundamental particles interact in four ways: By strong, electromagnetic, weak and gravitational interaction. Every hadron we know consists of elementary particles called quarks. There are six different quarks, that can be distinguished by flavor: up, down, strange, charm, bottom, and top quark and their antiparticles. Each quark posseses color charge (red, green or blue) that causes a strong interaction and leads to the formation of hadrons. This interaction is mediated by gluons that carry color and anticolor charge [2]. As described by quantum chromodynamics, the force becomes asymptotically weaker if the energy increases. At low energies like in a nucleon the interaction is so strong that this leads to a confinement of quarks and gluons which means that quarks can not exist unbound. The potential between a heavy quark-antiquark pair can be written as $V_{q\bar{q}}(r) = -4\alpha/3r + Kr$ [3], while the first $1/r$ term is the Coulomb like potential and the second one describes the constant force at large distances. If the radius is increased, the energy stored in the flux tube is sufficient to create a new quark-antiquark pair [4]. Thus it is impossible to separate quarks from each other at low energies. This is an explanation for the experimental observation that free quarks do not exist what is called confinement. However confinement is not yet understood at a fundamental level. In contrast at high energies the strong coupling constant α becomes smaller and thus quarks become asymptotically free [5].

A state with deconfined quarks and gluons is called the quark-gluon plasma (QGP) [6]. It is produced if nuclear matter reaches critical conditions in terms of temperature and gluon density. In such an environment the quarks are screened from each other. A QGP occured in the early time of our universe. In order to confirm theories of the quantum chromodynamics or to get new results, the properties and the evolution of the quark-gluon plasma has to be studied. In fact quantum chromodynamics can calculate the interactions of single quarks but if we look at a thermalized many-body system it is nearly impossible to compute all interactions by a model. This can be compared to quantum electrodynamics that can describe a hydrogen atom or a more complex water molecule but it can not deal with a many-body system like water, so it is not possible yet to get detailed information about viscosity of water or the phase diagramm just from the atomic theory. Analogous we can not only investigate the quark-gluon plasma theoretically. Instead of that we want to measure for example the viscosity, transport coefficients and the phase dependence from temperature and baryon density (chemical potential) [7]. This can be studied for example by measuring the energy loss of particles that go through a QGP, e.g. if a jet interacts with the plasma. Moreover the production and quantities of the J/ψ meson are studied to learn something about dissociation and

recombination of the heavy charm quarks in the QGP [8] [9]. Therefore especially the e^+e^- decay channel is used to detect them. In order to investigate all those issues, of course a QGP has to be created. A phase transition from the bound hadronic state to the QGP can happen if there are critical conditions like high temperature, energy and density [6]. This takes place when heavy nuclei collide, thus we will now look at heavy ion collisions. Today, the Relativistic Heavy Ion Collider at Brookhaven and the Large Hadron Collider (LHC) - described in the next chapter - do collider research on QGPs.

2 The ALICE Experiment at CERN

2.1 CERN accelerators

The European Organization for Nuclear Research (Conseil Européen pour la Recherche Nucléaire) known as CERN was founded in 1954 and is based in Geneva, Switzerland [10]. It consists of 22 member states and approximately 3200 employees [11]. Over time Cern invented lots of new techniques and as the most prominent one the World Wide Web can be mentioned that was developed 1989 by Tim Berners-Lee, a British Scientist who worked at CERN [12]. Moreover new detectors were developed like the multiwire proportional chamber [13] that was awarded in 1992 by a Nobel Prize to Cern staff researcher Georges Charpak and section 3.3 will deal with these multiwire proportional chambers. Mainly CERN built various particle accelorators like for example the Synchrocyclotron (SC) in 1957 or Linac 2 in 1978, an approximately 30 m long linear accelerator that accelerates protons up to 50 MeV [14] and is still in use today. It consists of cylindrical electrodes - also called Wideroe structure - that change frequently their charge. Instead of the SC, today the more powerful Proton Synchrotron (PS) is used. The PS is a ring accelerator that can increase the energy of protons up to 25 GeV and those of lead ions up to 5.9 GeV/u [15]. Together with the Proton Synchrotron Booster and the Super Proton Synchrotron (SPS), Linac 2 and PS build the preaccelerating complex for the Large Hadron Collider (LHC) in proton mode. In lead mode, the ions are firstly accelerated in the Low Energy Ion Ring (LEIR) and after that injected into the PS and SPS until their energy is about 117 GeV/u and they finally enter the LHC that will be described in section 2.2.

2.2 LHC overview

The LHC is the worlds biggest and most powerful accelerator located in an approximatley 26.7 km long tunnel 50 to 175 m below the surface close to Geneva [15]. It is built to accelerate protons and ions close to light speed so that collisions gain centre of mass energies up to $\sqrt{s} = 14$ TeV for proton-proton and $\sqrt{s} = 5.02$ TeV for lead-lead collisions [16]. In order to keep the beam in a circle, strong magnetic fields are required and therefore 1232 superconducting dipole magnets are installed which have to be cooled down to 1.9 K and reach a maximum field strength of 8.36 T [15]. Before particles enter the LHC they have to be preaccelerated. If they have reached a sufficient energy of 450 GeV for p-p collisions, they are injected into the LHC in bunches of around 10^{11} protons (in proton mode) and a length of a few cm. Together there are up to 2508 bunches in the beam which circulate with a frequency of approximately 11 kHz.

The LHC consists of two beam pipes in vacuum and the bunches orbit clockwise and anticlockwise so that they collide at four points every 25 ns which leads to a collision rate of 6×10^8 collisions/s [17]. At the collision points the detectors CMS, LHCb, ATLAS and ALICE are placed. The CMS experiment studies in general the supersymmetry, the collision of heavy ions and has discovered the Higgs boson. LHCb inspects the decays of hadrons that contain a bottom or charm quark and measures precisely their CP-violation. Similar physic contents as in CMS are studied in the ATLAS experiment. ALICE will be described more detailed in section 2.3.

2.3 The ALICE experiment

ALICE (A Large Ion Collider Experiment) is a part of the LHC facility at CERN. It is the worlds biggest experiment optimized to study heavy ion collisions at high centre of mass energies [18]. Overall the ALICE detector has a length of 26 m, is 16 m in diameter and its mass is about 10 000 t [19]. The central barrel is located inside a magnetic field of 0.5 T produced by solenoid magnet - see fig. 2.1. As described in section 2.2, protons and lead ions collide at the position of the ALICE detector. Due to the resulting high temperature and energy density about 8000 times per second (in Pb-Pb mode) a quark-gluon plasma is produced, that is expected to be similar to the conditions shortly (10^{-6} s) after the Big Bang. ALICE is able to observe the remnants of the plasma and study its properties that are important topics in quantum chromodynamics. Since a direct observation of the plasma is not possible due to its short lifetime of about 3×10^{-23} s [20], created particles like electrons, pions and photons are measured. The properites of these particles, like mass and momentum, are determined by several specialized detectors as explained in section 2.3.1.

2.3.1 Detectors

In order to distinguish and observe the produced particles, ALICE consists of various subdetectors as shown in fig. 2.1. They will be briefly described in the following. The Inner Tracking System (ITS) measures the exact position of the collision point by six cylindrical layers of silicon detectors. After that the Time Projection Chamber (TPC) [21], a large volume of 88 m^3 filled with a gas mixture of Ne-CO_2 or Ar-CO_2, measures the track. Charged particle ionize the gas inside the TPC along their trajectory and the created electrons drift towards the end plates of the cylinder due to an electric drift field of 400 V/cm. Close to the plates there are anode wires that cause an avalanche process and the produced positive ions induce a current signal on the pad plane where it is read out and then the track can be reconstructed. Moreover the magnetic field leads to a curvature of the tracks that is used to calculate the momentum of the particles. The next detector in a distance of 2.95 to 3.69 m [22] from the beam is the Transition Radiation Detector, that will be explained more detailed in section 2.3.2. Furthermore there is a Time of Flight (TOF) detector that is used to determine the velocity of the particles. Other detectors are the High Momentum Particle Identification Detector and various calorimeters.

2.3.2 TRD

The TRDs main purpose is to distinguish electrons and positrons from other charged particles by using the emission of transition radiation that is emitted when the particle crosses many layers of thin materials; this process will be described in a more detailed way in section 3.4.

The whole TRD consists of 521 detector modules, each containing a radiator and a readout chamber. They are ordered in 18 supermodules in azimuthal direction and each of them consists of 6 detector layers subdivided into 5 stacks in beam direction as shown in fig. 2.2. Each detector has 144 cathode pads in azimuthal-direction and between 14 to 16 pads in beam-direction so that in total there are about $1.16 \cdot 10^6$ readout channels. [23]

In order to understand the behaviour of the detector we have to look closer at the readout chambers. Mechanically the chambers are $37\,\mathrm{mm}$ long while $30\,\mathrm{mm}$ are the drift region and $7\,\mathrm{mm}$ are the amplification region that is separated by the cathode wire plane. The whole chamber is filled with a gas mixture of 85% Xe and 15% CO_2 [22]. Due to unavoidable small leaks it is not possible to have an exactly constant gas composition. This has a significant effect on the detector output as we will see later. The pressure inside the chamber follows the ambient pressure with a maximum overpressure of 1 mbar. This causes, that the output is pressure dependent, as we will show in a model in chapter 4 and with our experimental results in chapter 5. Moreover the pad plane and the wires can be deformed due to gravitation or other effects. This changes the electric field inside the amplification region and thus also has an influence on the output.

In order to understand how the TRD works the physics background of gas detectors will be explained in the next chapter in a more detailed way.
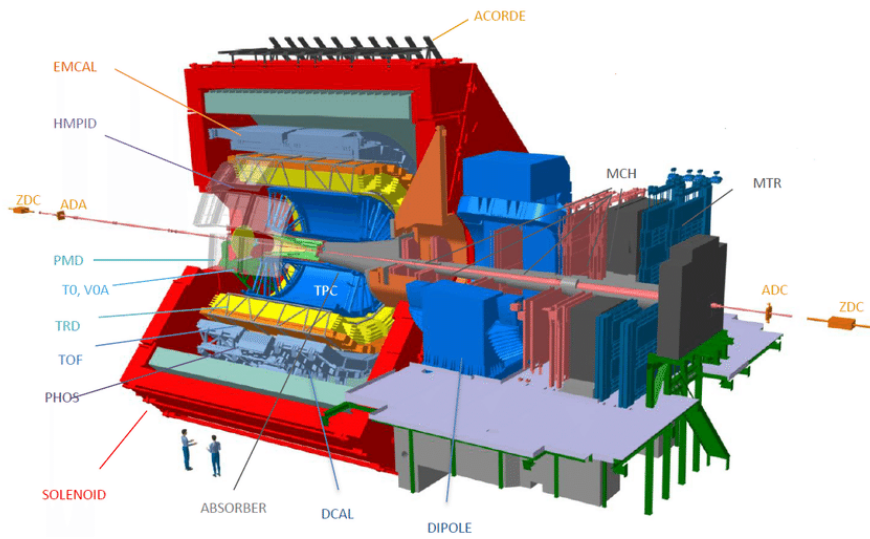
Figure 2.1: The detectors of the ALICE experiment are shown schematically . One can see the TRD and the outer magnet. For size comparison there are two human beings [24].
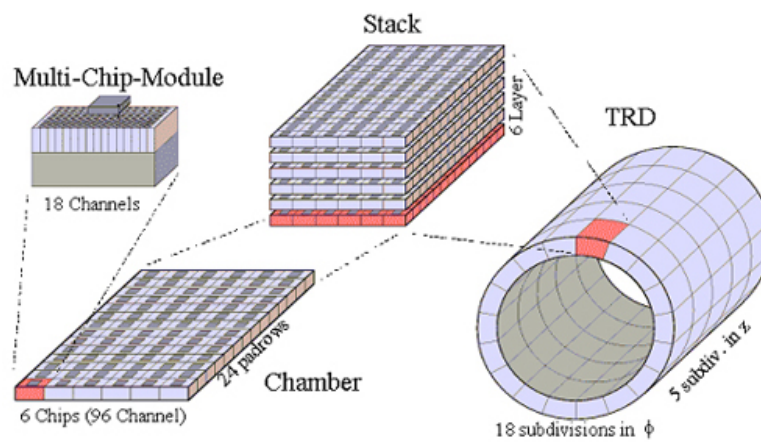

Figure 2.2: Right: The 18 sectors and 5 stacks in z-direction. In the upper part there is one supermodule consisting of 6 layers [23].

3 Gas detectors

3.1 General principle

There are different types of gas detectors: A basic one is the Geiger counter, which simply detects ionizing radiation. Others are more complex and allow the measurement of particle tracks and their specific energy loss like the TPC or the TRD. The basic principle of gas detectors is similar: Charged particles go through a drift volume and ionize a gas via energy loss which is described by the Bethe-Bloch formula 3.1. The generated charges drift in an electric field towards an anode wire that causes amplification. Then the signal and its position is measured [25]. First the energy loss of a particle that goes through matter will be described.

3.2 Bethe-Bloch formula

The mean rate of energy loss of particles that go through matter can be classically estimated by the calculation of Bohr. This calculation was expanded for relativistic quantum mechanics in 1932 by Hans Bethe which lead to the Bethe-Bloch formula [26] :

$$-\frac{dE}{dx} = Kz^2\frac{Z}{A}\frac{1}{\beta^2}\left[\frac{1}{2}ln\frac{2m_ec^2\beta^2\gamma^2W_{max}(M)}{I^2} - \beta^2 - \frac{\delta(\beta\gamma)}{2}\right] \qquad (3.1)$$

In this formula z is the charge number of the incident particle, Z the atomic number of the absorber, A the molecular atomic absorber mass, W_{max} the maximum energy transfer in a single collision (that is mass and energy dependent), I the mean excitation energy and δ is the density effect correction. In principle it is not easy to calculate I, thus estimates based on experimental data are widely used. The density effects takes into account that if the particle's energy increases, the electric field flattens due to relativistic effects and furthermore real media become polarized what limits this field extension. It is remarkable that the Bethe-Bloch formula does not depend on the mass of the projectile particle. The unit of dE/dx is given in MeVg^{-1}cm^2. If we are interested in the energy loss for a given material the equation needs to be multiplied with the density ρ; especially for gases the pressure dependence of the Bethe-Bloch formula is important. We have to keep in mind that the Bethe-Bloch formula only calculates the mean rate, so actually the energy loss is Landau distributed and the most probable loss is smaller than the mean.

This equation is valid for particles in an energy range of $0.1 < \beta\gamma < 1000$ and is accurate in the order of a few percent. However for electrons the Bethe equation can not be used because their low mass leads to a more significant energy loss by Bremsstrahlung

that is not regarded in the formula and furthermore they are not distinguishable from valence electrons.

The $\frac{1}{\beta^2}$ term shows us that slower particles lose more energy. We can find a minimum value of dE/dx at $\beta\gamma \approx 4$ and particles that have an energy in the range of the minimum are called Minimum Ionizing Particles (MIPs). If the speed of the particle is increased then radiation effects like Bremsstrahlung, e^+e^- pair production and photonuclear interactions become more important, thus above approximately $\beta\gamma = 1000$ the Bethe-Bloch formula is not correct any more [26]. So we have to consider that this forumula can only be used for moderately relativistic particles but fortunately the particles we want to inspect are in the velocity range which is described by Bethe-Bloch formula.

3.3 Multi-wire proportional chamber

3.3.1 Design

A single wire counter can detect radiation and measure its energy but to get the position and track of a particle over a large area one needs multi-wire proportional chambers. Generally it is built by lots of parallel anode wires that are at a positive potential inbetween two cathodes [25]. The electric field close to the wires is a radial field but at larger distances it is nearly homogeneous. To improve the homogeneity of the (drift) field in some detectors like the ALICE TRD there are also cathode wires that separate the drift region from the amplification region [22]. The cathode is divided into small stripes perpendicular to the wires so that the induced signal in the wire and cathode allows to determine the position of the particle - see section 3.3.2. Now we want to look how the signal in a drift chamber detector is generated.

3.3.2 Signal generation

If the particle crosses the drift region this leads to ionization as described in section 3.2. The induced primary clusters drift because of the electric field toward the anode wires with a nearly constant drift velocity due to collisions with gas atoms [25]. Because the velocity is constant a measurement of the drift time allows the calculation of the point of ionization. During the drift, the primary electrons lose energy due to collisions and some electrons are completely lost due to recombination of electrons and ions or electron attachment [25] but this effect is only in the order of $10\,\%$. If we are interested in the exact ionization position we have to consider diffusion that leads to a spread of the charge cloud. As mentioned above the electric field close to the wire is a radial field that is proportional to $\frac{1}{r}$ thus it is very large in the vicinity of the wire. Because of that electrons gain sufficient energy so that they can ionize atoms and this generates secondary electrons which can again lead to ionization. This process is an electron avalanche that leads to an amplification of the signal in the order of $10^4 - 10^5$ [25]. The number of electrons as a function of the distance from the centre of the wire (r) can be described by an exponential function with the Townsend coefficient as parameter [28]. I will discuss this in more detailed in chapter 4 where I model the number of electrons as

a function of r by considering the attenuation effects in the drift chamber as well as the amplification by the Townsend coefficient.

The readout of the signal can be done in different ways. Some multi-wire proportional chambers measure the current in the anode wire or the induced signal on the cathode pads after the positive ions drifted to it. Furthermore it is possible to detect the image charge that the electric field of the positive ions induce on the cathode [23]. A general advantage of the cathode pad readout is the good spatial resolution. To improve this resulution the so called center of gravity method is used that utilizes the signals of more than one pad to localize the center of ionization with an accurancy of approximately 50 μm [25].

3.4 Transition Radiation Detector

In this section I will describe the principle of a Transition Radiation Detector (TRD) and more specifically refer to the TRD of the ALICE experiment [22]. If a highly relativistic charged particle crosses the boundary between two media of different dielectric constants, a photon can be emitted. Its energy is proportional to the Lorentz factor γ. Those photons ionize the gas in addition to the charged particle, which leads to an average larger signal. Thus it is possible to discriminate the faster electrons especially from pions. In order to increase the possibility of producing a photon, we use stacks of a few hundred foils in the radiator. After that both the TR photon and the particle have to be detected in the chamber. In fig. 3.1 you can see two particles that cross the drift region and produce primary clusters along their path. Additionally the electron generates transition radiation that causes another cluster at the beginning of the drift region. In order to absorb the photon, xenon is used because its absorption length is in the order of 1 cm so that the photons are mainly absorbed directly at the beginning of the drift region and lead to ionization. As a consequence the signal vs time as plotted in fig. 3.2 will show a peak at later times if we look at electrons that cause transition radiation because the TR photons are generated most distant from the anode wires so that their cluster will appear later at the anode wire. That's one possibility to distinguish for example pions from electrons. Furthermore the average pulse height is lower for pions because of their lower energy loss in the regarded momentum range. One could suggest that thus it might be quite easy to distinguish particles and measure their correct properties but that presupposes that every detector gives the same output for every condition. However the signal of a gas detector depends on different parameters: pressure, high voltage settings, gas composition and variations in the electric field due to geometrical reasons. As a consequence a complex calibration of the TRD is necessary. In this thesis an improvement of the present TRD calibration is discussed. First of all I want to understand the pressure dependence of the gain that is modeled in chapter 4.
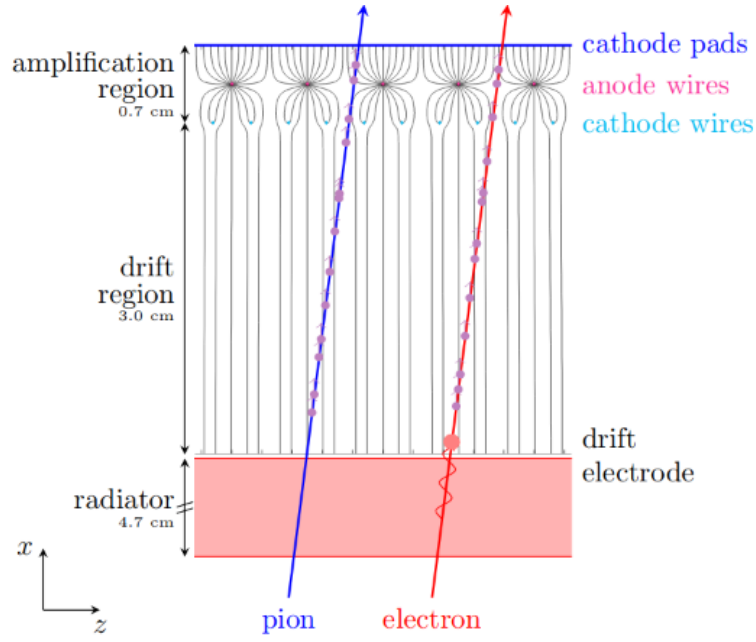
Figure 3.1: A pion and electron crossing the TRD. In the drift region both of them ionize the gas and generate clusters which drift towards the anode wires. Because the electron produces transition radiation and these photons are absorbed directly in the gas there is another cluster for electrons [23].
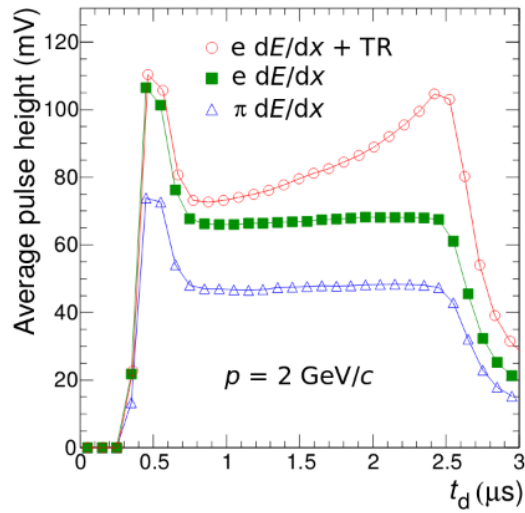

Figure 3.2: The average output signal is shown for electrons with and without transition radiation (TR) and for pions. The amplification peak shows up at $\approx 0.5\,\mu$s If we look at electrons with TR then a second peak is clearly visible [23].

10

4 Model of pressure dependence of the gain

Experimental results show us [29], that the gain is inversely dependent on pressure. In the following the processes inside the detector are modelled in order to be able to explain the pressure dependence.

4.1 Four sub-ranges for gain generation

- If a particle flies through the detector it generates electrons through ionization during the whole distance.

  First we want to look only at the electrons that are generated within the first 5 mm. Their number increases linearly with distance as described by the Bethe formula. It is also linearly pressure dependent as explained in section 3.2 because $\rho \propto$ pressure if we assume the ideal gas law. So, at an increased pressure, the straight line that describes the number of electrons as a function of distance has a higher slope.

- After that the number of electrons is attenuated because they are absorbed mainly by O_2 [22]:
$$N(t_{\mathrm{drift}}) = N(0) \cdot \exp(-p \cdot p(0_2) \cdot C_{\mathrm{att}} \cdot t_{\mathrm{drift}}), \qquad (4.1)$$

  while p is the total pressure, $p(O_2)$ the partial pressure, C_{att} the attachment coefficient (that depends on gas mixture) and t_{drift} the drift time. It is also pressure dependent, thus approximately $N \propto exp(-p^2)$. For higher pressures the attenuation is stronger (see formula) but the main attenuation is quite small for TR-detectors (in the order of 10 %) because the drift distance is usually only a few centimetres. Therefore this exponential attenuation can not explain why the experiment shows us that the signal decreases with increasing pressure.

- We have to consider other effects: Close to the anode wire starts an avalanche process which is described by the Townsend coefficient [28]:

$$ln(G) = \int_a^b \alpha \mathrm{d}r, \qquad (4.2)$$

  where G is the attenuation factor and α is the Townsend coefficient. The integration has to be done from the surface of the wire a to a distance where the electric field is so weak b that it doesn't contribute to the amplification any more. This Townsend

coefficient has to be divided into two coefficients α_1 and α_2 for ranges more distant and really close to the wire [28]. In order to distinguish these ranges we define λ_i the electron path that is required to gain enough energy to ionize atoms. If we are close to the wire, then λ_i becomes smaller due to the high electric field and $\lambda > \lambda_i$. In this range the Townsend coefficient is α_2:

$$\alpha_2 = \frac{1}{\lambda} = n\sigma \propto p \tag{4.3}$$

while n is the particle density, σ is the total cross section and p is the pressure.

- More distant from the wire $\lambda < \lambda_i$ thus usually an electron can not ionize a gas molecule within its free path. We have to think about the chance that the free path is longer than λ_i and multiply it by the number of mean free paths per unit length. This is done in α_1:

$$\alpha_1 = \frac{1}{\lambda} \cdot \exp\left(-\frac{\lambda_i}{\lambda}\right) = \frac{1}{\lambda} \cdot exp(-\frac{V_i}{\lambda E}) \tag{4.4}$$

V_i is the effective ionizing potential and E the electric field.

Because $\lambda = \frac{1}{n\sigma}$ and $n \propto p$ the second Townsend coefficient rises linearly with pressure, but the first one decreases with higher pressure. Thus the first Townsend coefficient can explain the inverse pressure dependence of the gain.
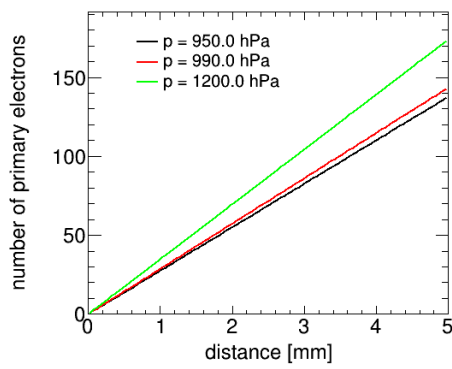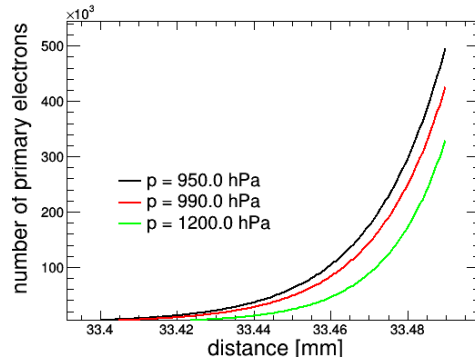
(a) Produced electrons by ionization in the first 5mm.
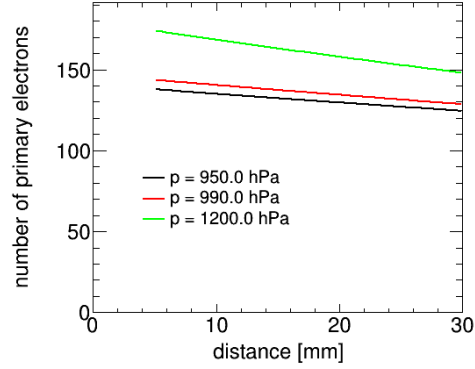
(b) Attenuation due to oxygen in the drift region.
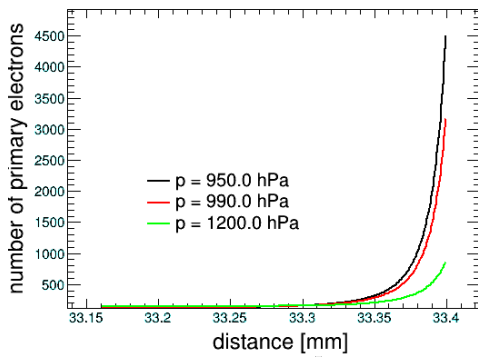
(c) Amplification because of first Townsend coefficient.

(d) Amplification due to second Townsend coefficient.

Figure 4.1: One can see the 4 different processes that influence the number of electrons for 3 different pressures. The normal pressure range goes approximately from 950 mbar (black) to 990 mbar (red). In order to show the effects better an extreme pressure value of 1200 mbar (green) is plotted as well. In (d) the value of each curve at x=33.49 mm (surface of the wire with radius 10 μm) is mainly important for us because it is proportional to the gain that is measured.

The model is based on formula 3.1, 4.1, 4.2 and the two Townsend coefficients. In the following is described how the parameters for the model were determined in order to fit the experimental results.

We know that within 1 cm approximately 275 electrons are generated [22] due to energy loss, so the number of electrons as a function of distance was written as $N(x) = mpx$ with the pressure p, distance x, and the parameter m. This is plotted in fig. 4.1a for three different pressures. I estimated the attenuation as $N(x) = A \cdot exp(Bp^2x)$ and set the parameter A so that at x=5 mm the value fits to the number of produced electrons by energy loss. This is a simplified procedure because the electrons that were directly produced at x=0 are also attenuated during the first 5 mm but in fact this is negligible

since the attenuation is only in the order of 10 % and not the relevant effect for the pressure dependence. The attenuation can be seen in fig. 4.1b

In the model the amplification due to the first Townsend coefficient starts at the beginning of the amplification region of x=30 mm but a significant amplification can only be seen in the last 1 mm thus only this range is plotted in 4.1c and 4.1d. Now for small steps in Δx the amplification factor M is calculated by the integral 4.2 with $\alpha = \alpha_1$ and so iterative the number of electrons is estimated. The first Townsend coefficient used in this calculation is estimated by $\alpha_1 = p \cdot A \cdot exp(-B/S)$ while A and B are parameters and $S = E/p$. E is the electric radial field that can be calculated: $E \propto HV/r$.

In nearly the same way fig. 4.1d was created by using α_2 and performing the iterative calculation in the range closer to the wire.

The most important result of this model can be seen in 4.1d. Although at higher pressures more electrons are produced due to the higher primary ionization and the amplification by the second Townsend coefficient is stronger we get a lower number of final electrons for higher pressures. This happens due to the first Townsend coefficient that is inversely pressure dependent and can explain our experimental result that the gain decreases with increasing pressure. That will be studied in more detail in section 4.2.

4.2 Gain vs pressure

We are interested in the final number of electrons, which is proportional to the gain, as a function of pressure.
Each of the 4 processes depends on the pressure in different ways. The first Townsend coefficient $\alpha_1 \propto p \cdot exp(-p)$ has to be integrated while the integral ranges depend on the pressure as well, because $\lambda = \lambda(p)$ while λ_i is constant. Moreover we are interested in the pressure dependences for different TRD pads. At a reference pressure they have different gains due to the variance of the electric field. This field varies because of geometrical reasons or different high voltages. Due to that we estimated, as discussed in chapter 4, the gain as a function of pressure numerically and varied the high voltage in order to simulate a variation of the E-field: This is shown in fig. 4.2.
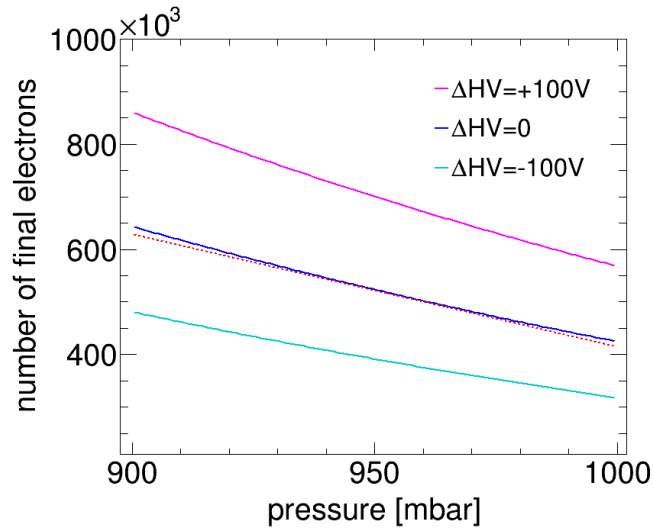
Figure 4.2: Pressure dependence of the final number of electrons for three different E-field strengths. The dashed red line is a straight line to guide the eye.

As we see, the pressure has a significant effect on the gain and furthermore the gain varies in a different way if we start at a different gain at a reference pressure. The curves seem to be exponential ones although as described above various effects contribute. Actually the real pressure range is smaller than shown in fig. 4.2 so that it is also possible to approach the curves as straight lines with different y-intercept and slope. As shown later it is even better to treat them as exponential curves of the type $N_{\text{final}}(p) = A \cdot exp(Bp)$. Then we need to discuss whether A and B are both free parameters or if we should fix the slope B.

4.3 Linear and exponential fit

First of all we vary in the model the electric field in continuos steps to get data points for the number of final electrons N_{final} at different pressures for various electric fields.

If we look at fig. 4.2 in a closer, more realistic pressure range, we see that the curves seems to be approximately linear. That is the reason why we first try a linear fit. Every linear fit results in a different slope and y-intercept. In a wider pressure range a clear deviation from a straight line is observed. Due to the exponential behaviour of the first Townsend coefficient, an exponential fit is also used. In fig. 4.3 one can see the data points for four example high voltages with exponential and linear fits. In the given pressure range both fits are a good description of the simulated points because the straight line fits only deviate by maximum 0.3% from the data points and the exponential fit only by less than 0.1%. Our result is that the slopes (B) of the exponentials are exactly the same while the coefficients A vary. This is a significant advantage and simplification

over the straight-line fits. The result that the slopes are constant is not trivial because the two Townsend coefficients depend on the electric field strength and furthermore the integration limits change as well. A qualitative explanation would be that B describes all processes that influence the gain but they do not depend on the electric field. Instead of that the electric field only changes the gain at a reference pressure so that in our model only A is changed. We have to be careful with that result because as I mentioned before the model simplifies a few. As a major result for experimental data we keep in mind that in the model the gain dependence on pressure can be fitted with an exponential curve and furthermore if we change the E-field then the slope of these exponentials should stay the same.
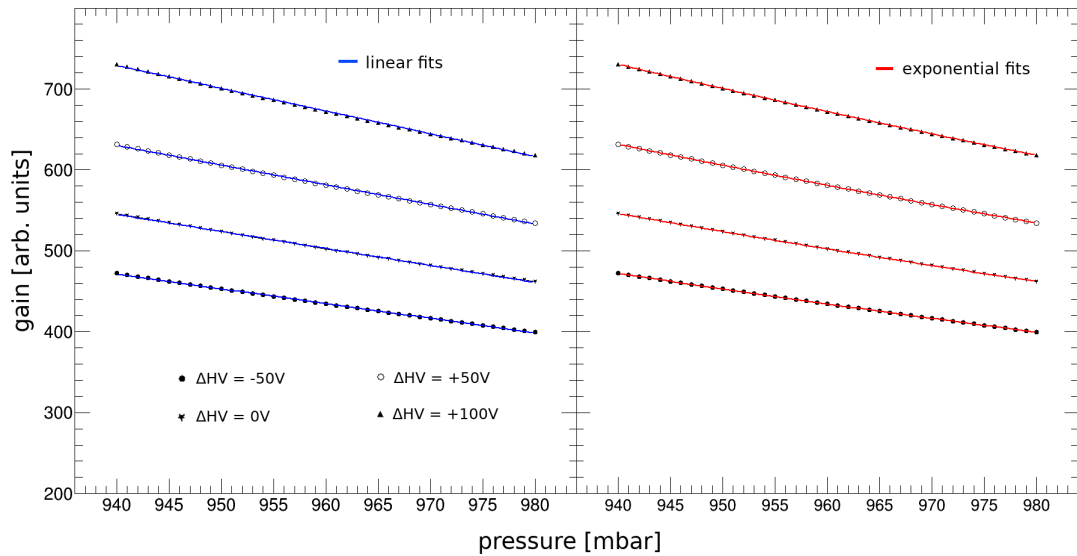
Figure 4.3: Simulated gain vs pressure for 4 different electric fields with fits. In the left part one can see the linear fits while on the right part the exponential fits are shown.

5 Pressure calibration

In the past the pressure correction was done once for the whole TRD. After that it was improved and applied to each of the 521 detectors by averaging the gain of each chamber [30] [31]. However the gains within each detector vary significantly as will be shown below. This causes that the pressure dependences are different due to the exponential curves and also the ratio between pads changes. Therefore it would be optimal to do a pressure correction as presented in chapter 4 for every single pad. The calibration is done by using Krypton decay data, as described in section 5.1.

5.1 Krypton calibration theory

In order to get data for the calibration, a Krypton run was done at the beginning of the year 2018 data taking period. For detailed information see [32]. During the run ^{83}Rb was placed into the gas stream. It decays into metastable ^{m83}Kr by β decay [33]. This Krypton disperses through the whole TRD gas volume so that it is distributed simultaneously. Actually the lifetime of $2.64\,\mathrm{h}$ of ^{m83}Kr is good because it is short enough so that the chamber can operate normally after a few lifetimes, but long enough to be distributed in all chambers.

The kryton run lasted from 17th to 26th of March 2018. In the first two days the solenoid magnet was turned off so these runs are not used in the following. From run id 283781 to 283889 the first supermodules were filled and then until run id 284036 the second supermodules were measured. In this period of time the pressure and the gas composition changed so that the data can be used for pressure calibration. On 26th of March the high voltage was varied while the pressure was nearly constant so these data will become important in chapter 6.

Krypton decays most probably to the level of $41.55\,\mathrm{keV}$ as shown in fig. 5.1. Then there is a cascade decay via the $9.39\,\mathrm{keV}$ level. Due to the short lifetime of this level the summed decay energy is collected in one cluster [32]. The emitted electrons have a concrete energy loss in the TRD so that they can be used for calibration purposes. A cluster finder is used to sum up the recorded charges of different pads to clusters. Then Krypton spectra are recorded for each pad. The background is rejected by using the timing information of the clusters [34] see fig. 5.2. Moreover it is checked that there is no calibration offset. In the following the position of the main krypton peak that corresponds to the $41.55\,\mathrm{keV}$ electrons will be used.
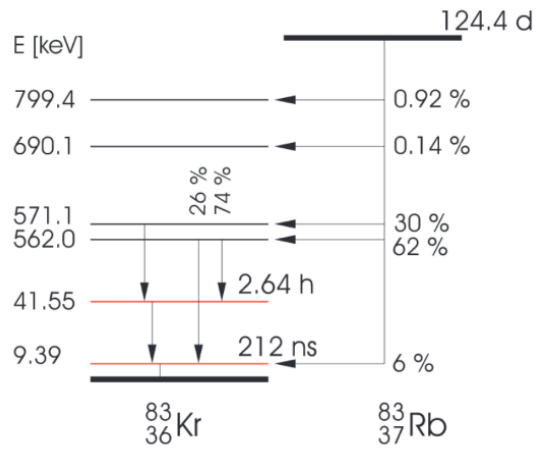
Figure 5.1: Energy levels of Rb and Kr. The most probable decay is that from $562.0\,\mathrm{keV}$ to $41.55\,\mathrm{keV}$ [33].
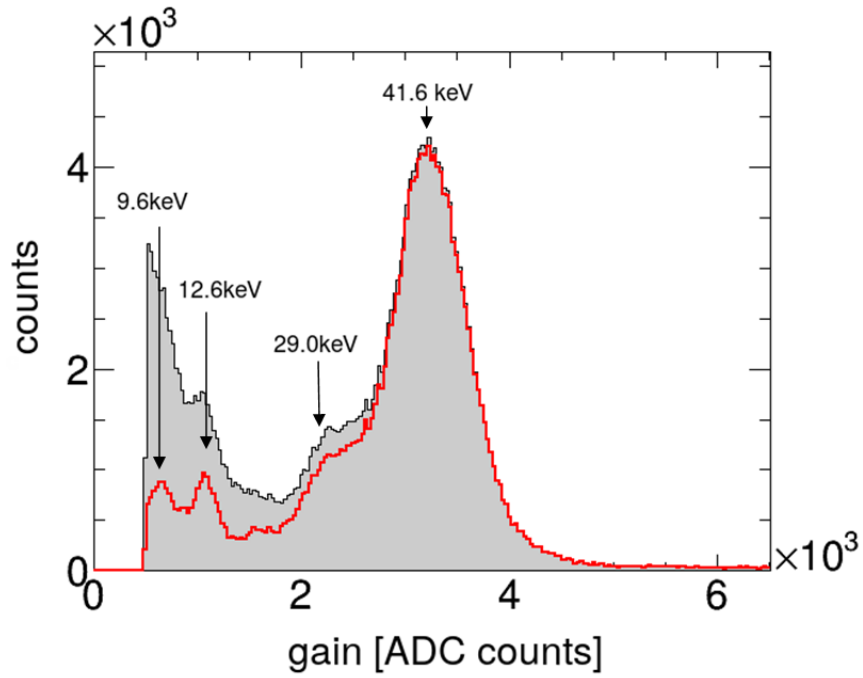

Figure 5.2: The pulse height spectrum of one detector before (grey) and after (red) background rejection [34]. One can see the main krypton peak at $41.6\,\mathrm{keV}$ and other peaks - for detailed information see [32].

5.2 Mean gain variation

At the beginning we study the main krypton peak position distribution for all TRD pads. For this the main krypton peak is fitted with a Gaussian, as shown in fig. 5.3.
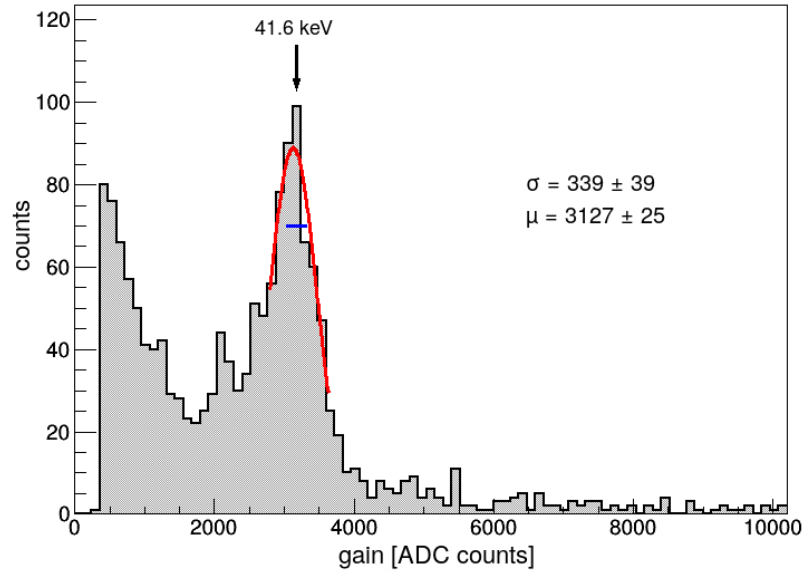
Figure 5.3: An example krypton spectrum of one pad is shown. A Gaussian fit (in red) was done in order to get the mean of the main Krypton peak. The arrow shows the maximum bin that was used as start parameter for μ and the blue line shows the start parameter σ. The fit result is listed.

The mean of the Gaussian for each pad is plotted in fig. 5.4.
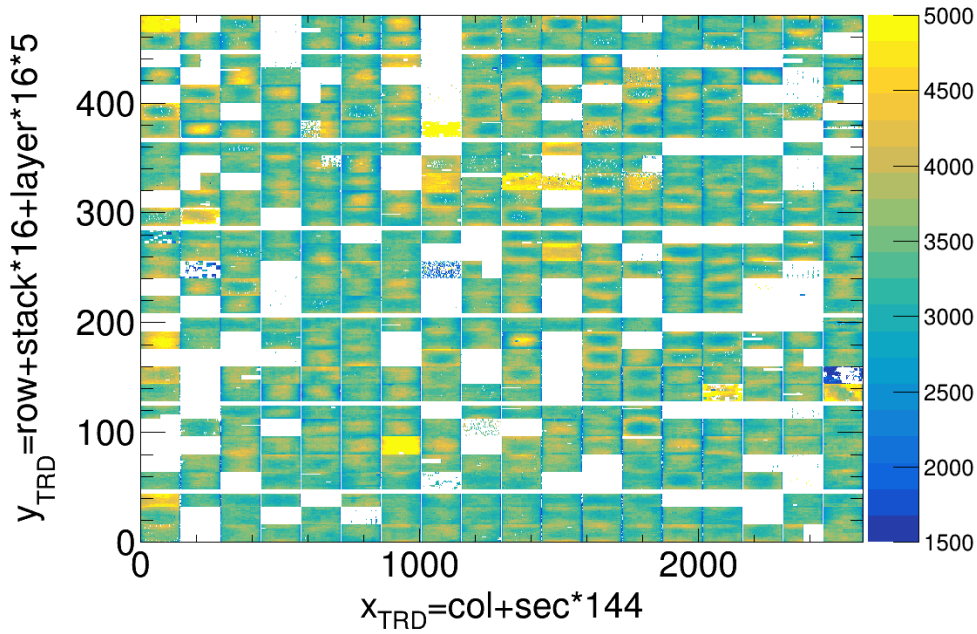
Figure 5.4: The mean position of the main krypton peak is plotted for all pads. One can see the variation over a large range (2000-5000 ADC counts) even within a detector [34].

The variation of the pulse height values (in ADC counts) shows that it is not sufficient to calibrate each detector as a whole, because in that case one would use the mean of the pulse height at a reference pressure value to do the calibration. But in fact the pads with different gain will depend on pressure in another way (as described in chapter 4) so that the result will deviate significantly.
In order to get to an improved calibration we will first look at a single detector.

5.3 Single detector

We first look at a single detector - for example detector 11. As one can see in fig. 5.5a and fig. 5.5b the gains within one single detector can vary over a large range, probably due to geometrical reasons like the bending of the cathode plane that influence the electric field. Now we divide the pulse height distribution in 3 categories so that each category has the same number of pads - see fig. 5.5b and additionally fig. 8.1. In order to study the pressure dependence we do the Gaussian fits for runs with different pressures and look at the gain for each category. More precisely we sum up the Krypton spectra of all pads of one category at a single pressure value in order to get sufficient data. Then we perform a Gaussian fit that gives us the gain for the main krypton peak. This is done for different pressure values and the data points we get are plotted in fig. 5.6. Because

20

the dependence seems to be linear a straight line fit for each category is done. As one can see the curves have a different slope as descriped in section 4.2. This motivates us to do the pressure calibration in that way.
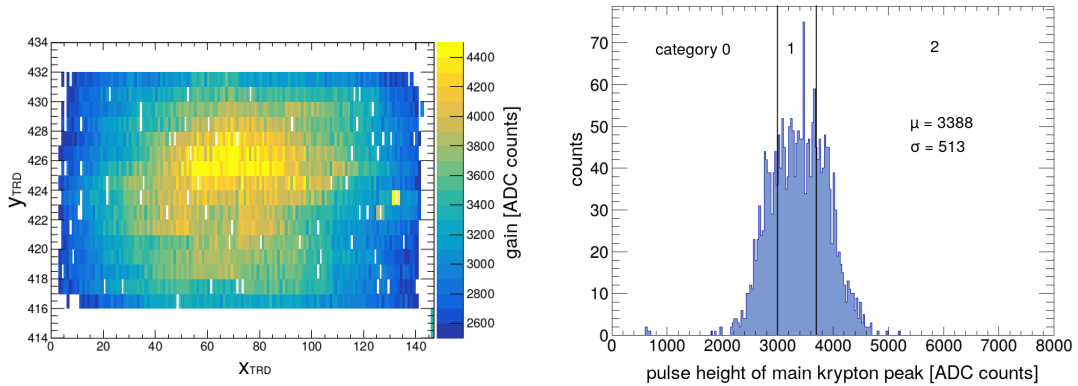
(a) The gain values of the main krypton peak are plotted for detector 11. We can see that they vary within the detector. Furthermore the higher pulse heights can be found in the middle of the detector what demonstrates us that the variation is due to geometrical reasons.

(b) The gain variation within detector 11 is plotted as a 1D histogramm. One can see that the ADC range is quite big. The relative rms of 15.1 % meets the technical design report. We divide it in 3 categories as indicated by the lines.
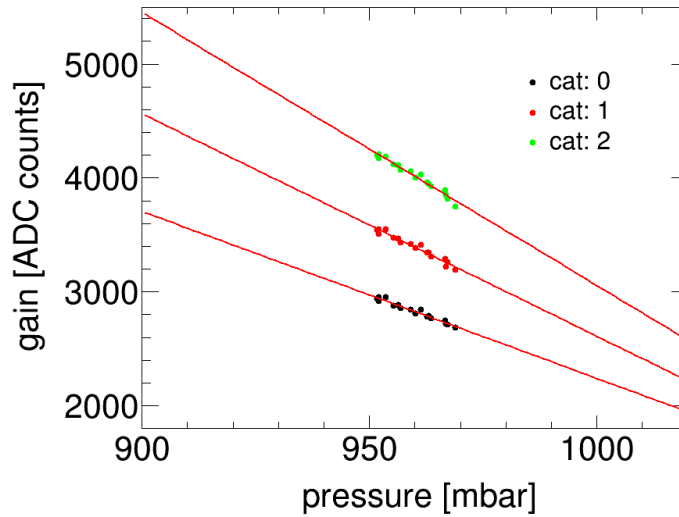
Figure 5.6: The gain of the main krypton peak for each category for different pressure values. The curves are straight line fits. An enlarged x-axis range was chosen in order to show that the straight lines aren't parallel.

5.4 All detectors

As a next step the procedure as described in section 5.3 is generalized: We look at the gain variation for each detector and partition it into 5 gain categories so that each category has the same number of pads. The variation and separation is shown for some example detectors in fig. 5.7. One has to keep in mind that the categories correspond to the gain but they were made for each detector independently so that a category does not mean the same gain range for each detector. That is the reason why one can not directly compare categories of different detectors. In fig. 5.8 one can see the result of the categorization. Generally this plot looks similar to fig. 5.4 but instead of a gain as value we now have a concrete category for each pad.
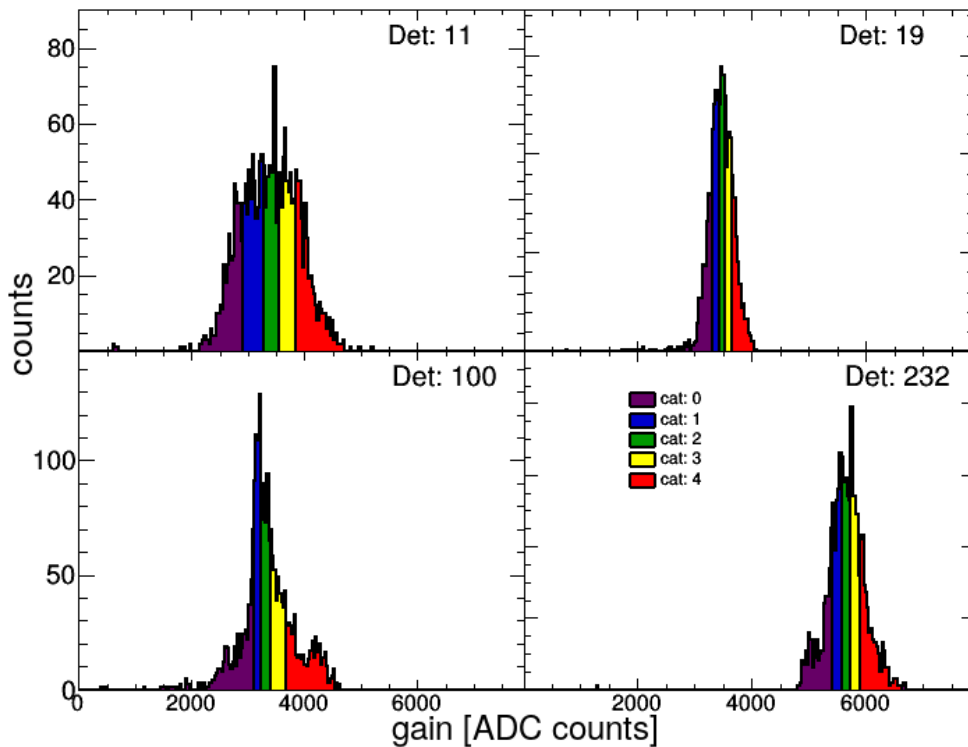
Figure 5.7: The gain variation for some example detectors. Due to geometry each detector is different. Every chamber is partitioned in gain categories with the same number of pads as indicated by different colors.
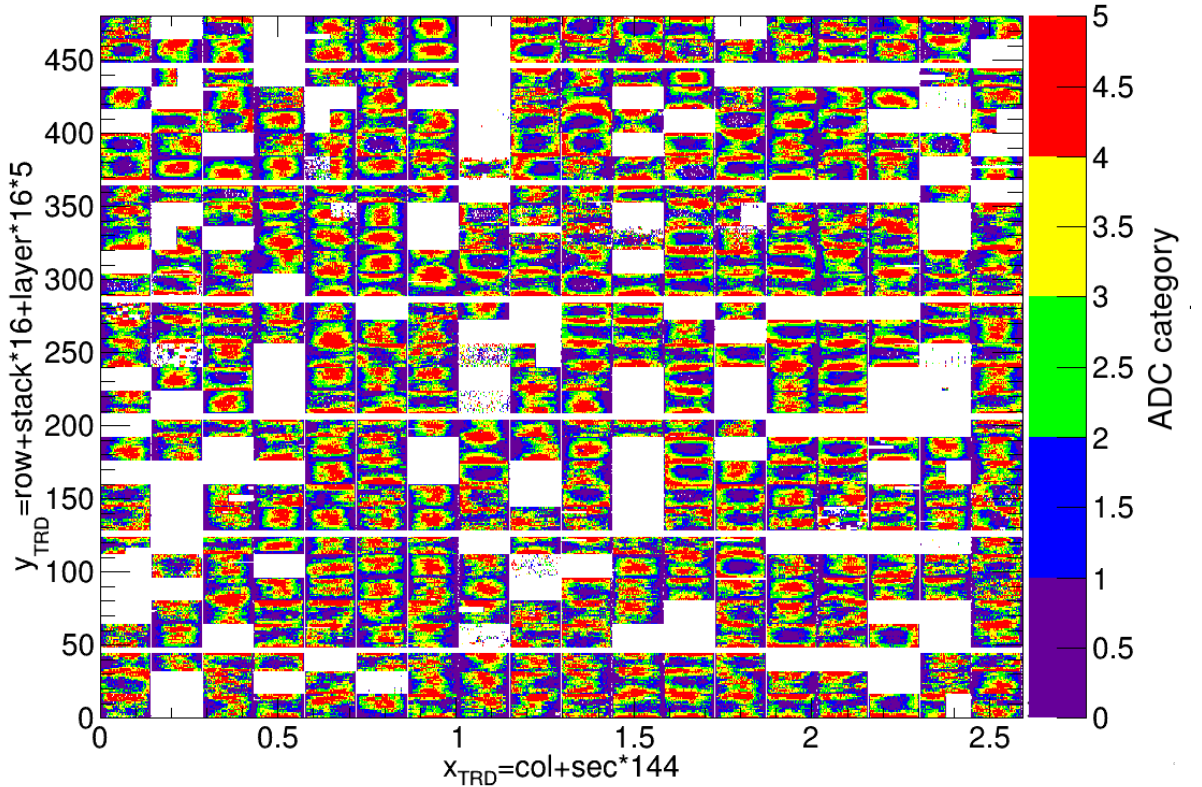
Figure 5.8: Distribution of the five ADC categories for all TRD detectors.

We now choose more than 3 categories in order to increase the precision. The best way to do the pressure calibration would be to do it for every pad on its own, but there is not a sufficiently large data set to get a good krypton spectrum for every pad and pressure value. Thus we look at one detector and sum up the krypton spectra of each catergory at one pressure value like it was done before. More than 5 categories are of course possible, but would not significantly improve the result.

Now we want to study the pressure dependence of the gain and therefore find the main krypton peak by a Gaussian fit . First it was checked whether the fit worked and moreover if some pads were defect so that they fire continously. As an effect the resulting krypton spectra had to much background and had to be filtered out by looking at the number of entries - see for example fig. 8.4.

One systematic uncertainity is that the peak position does not exactly represent the mean of the peaks of each pad because they were summed up. We try to estimate this uncertainty by calculating the relative difference of the maximum bin position to the mean of the Gaussian - see section 5.7 and fig. 5.16.

With the Gaussian fit we get the gain for each detector, category and pressure. The gain vs. pressure is shown for some example detectors in fig. 5.9.
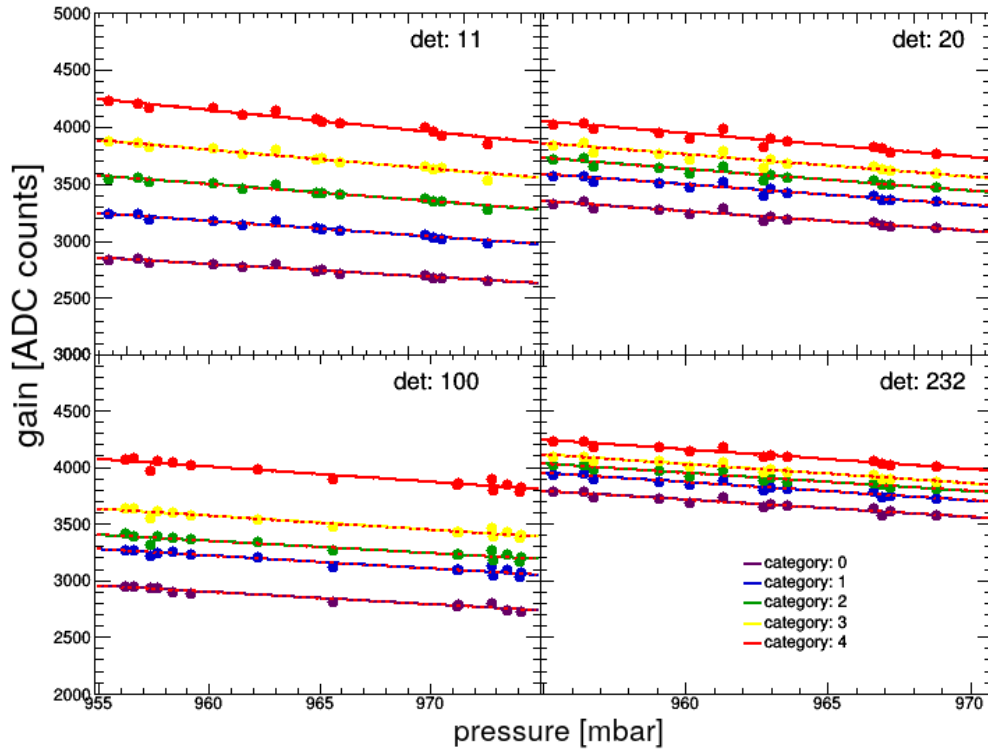
Figure 5.9: For some example detectors gain vs pressure is shown for the five ADC categories. The solid lines are straight line fits and the dashed red lines are exponential fits.

In fig. 5.9 straight lines and exponential fits are shown. Theoretically an exponential fit would be the better description, but as one can see a straight line fit is precise as well. It will be discussed in more detail in section 5.6.

5.5 Gas composition

We know that during the Krypton run the gas compostion wasn't constant and this might have an influence on the gain and furthermore on the way the gain changes. Thus we look at the gas compostion.

In fig. 5.10 one can see how CO_2, Xe, N_2, O_2 and H_2O change with run id (time). Furthermore the pressure is plotted and it is obvious that H_2O and O_2 follow the pressure. There is a step for N_2, Xe and CO_2 due to a gas leak during the run and we assume that this has a major influence on the gain although the gas composition changed only in the order of 0.1% or less. In order to exclude the influence of the gas composition on the gain we chose ranges in which the composition doesn't change a lot. For section 5.6 we used 6 ranges (shown in the H_2O plot) and for section 5.7 only two ranges C and D were used because there the gas compostion was more constant. Range C is before the

mentioned step and D after it. Moreover the relative fractions of H_2O and O_2 are quite constant in both ranges.
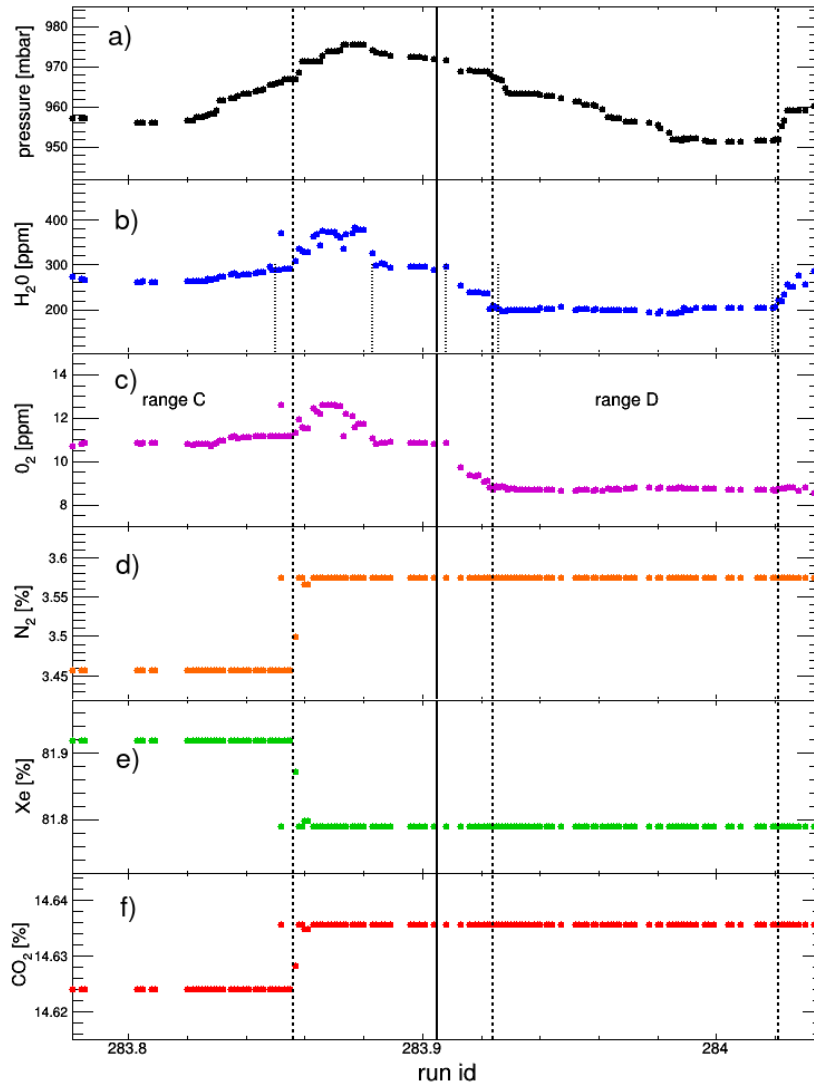

Figure 5.10: During the krypton run the gas composition changed and this is shown here for the main gas components. Furthermore one can see how the pressure is changing. The big black line shows the two different periods of calibration runs when half of the supermodules where filled and the dashed lines mark ranges C and D that are relevant for section 5.7.

5.6 Straight line fit

We first do a straight line fit withouth considering the gas compostion. The procedure is shown in fig. 5.9. Then we look closer at the parameters slope s and y-intercept b of the curves. We found that the y-intercept goes linear with slope. This can be seen in fig. 5.11. The units of y-intercept [ADC counts] and slope [ADC counts mbar^{-1}] are not shown in the following graphs for simplification.
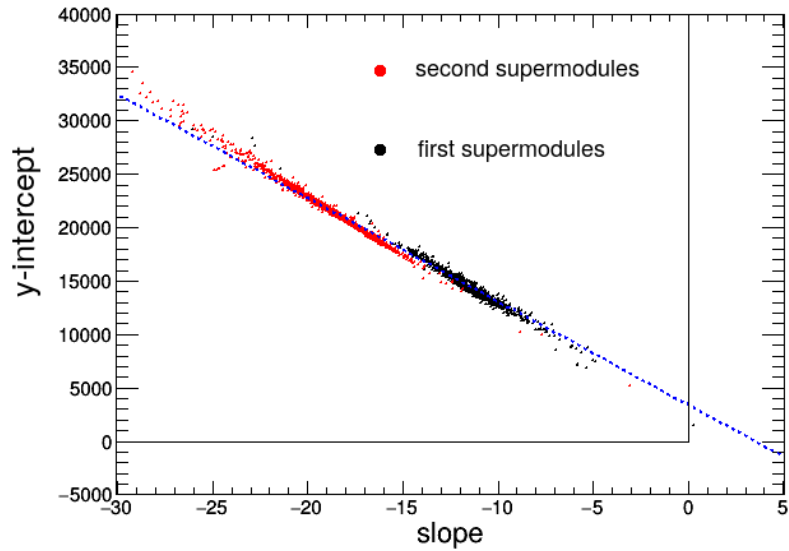

Figure 5.11: Fit parameters slope s and y-intercept b for all detectors. The colors mark the supermodules that had different gas compositions. A straight line fit to all data points is shown by the dashed blue line.
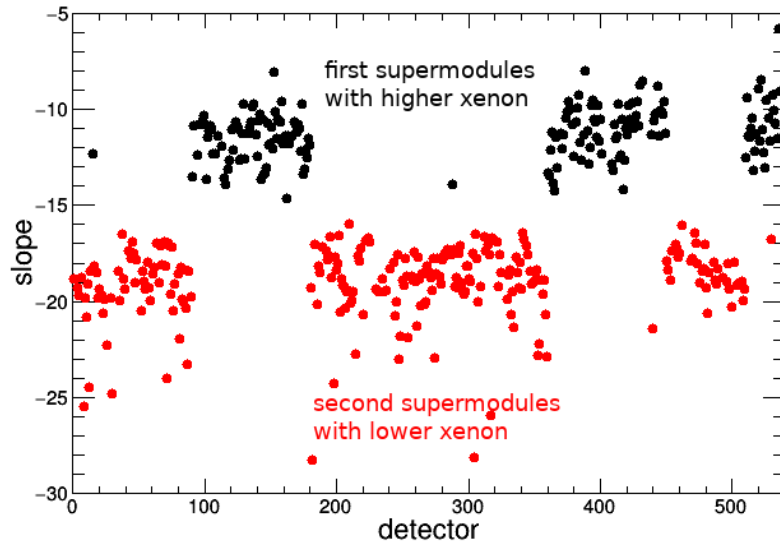
Figure 5.12: The slope of category 2 is plotted against the detector number. We see that the supermodules (marked with colors) have different slopes due to the different gas compositions.

Our first thought was that the ratio $r = \frac{\text{y-intercept}}{\text{slope}}$ might be constant but this is not the case since the straight line fit (fig. 5.11 in blue) does not go through the origin and furthermore it looks like there are actually more straight lines which overlap around $s = -15$. This can be explained by the gas composition which influences the gain. We know that the supermodules had different gas compositions during the krypton run - see 5.10. The supermodules with lower xenon (higher nitrogen) composition have a higher absolute slope what can also be seen in fig. 5.12 and they are marked in red.

As a next step we want to investigate the influence of the gas composition in a closer way and therefore we divide it in 6 ranges as shown in fig. 5.10b. Then we make the graph gain vs. pressure again but now not only for each detector and category but also for each gas composition range. After that again straight line fits are made but now for approximately constant gas compositions and you get again slope s and y-intercept b of these linears. After that the y-intercept vs slope is plotted and each gas composition range is marked by different colors. The result is shown in fig. 5.13. One has to pay attention that the curves are shifted in order to distinguish them. Apparently the gas composition has an influence on the curves especially on the variation of higher or lower slopes. Due to limited data, the gas compostion can not be analyzed in more detail using only the krypton data.

To sum it up although there is an influence of the gas composition it is possible to do a global fit in the y-intercept b vs slope s graph that will be later used in equation 5.2 because fortunately the curves in fig. 5.13 don't diverify that much. Anyway as will be shown in the next section an exponential fit is the better description.
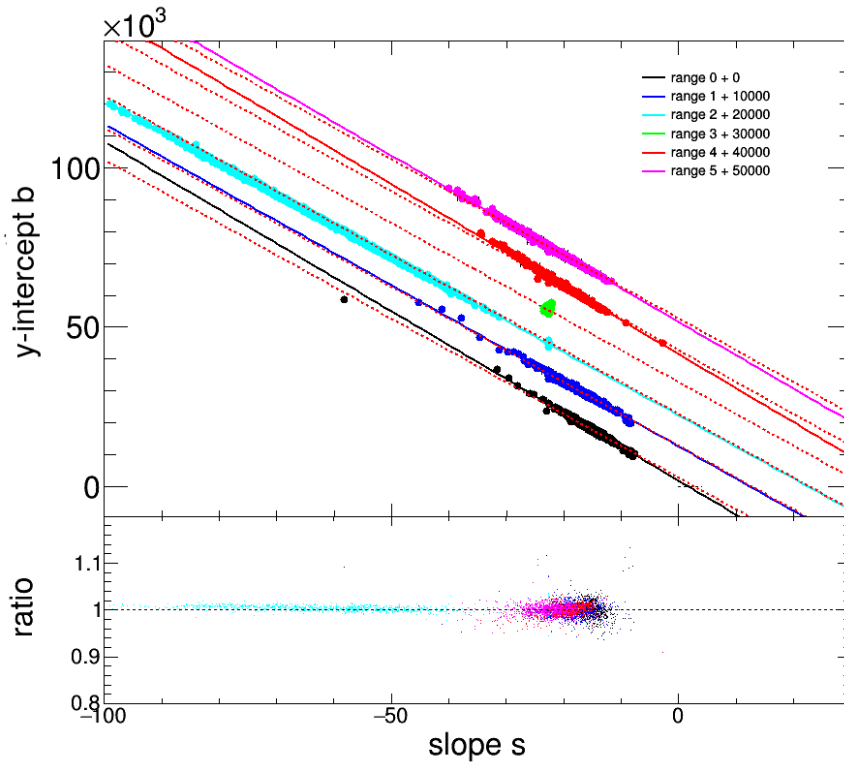
27

Figure 5.13: For each gas composition range the y-intercept vs slope is plotted. The curves are shifted for better visibility. The red dashed line is a straight line fit for all data points (also shifted) and the bottom graph shows the ratio between the global fit and single data points.

By this fit we get the parameters slope m and y-intercept c. In order to avoid misunderstandings I sum it up: In the gain vs. pressure graph we do linear fits as shown in fig. 5.9 and get fit parameters slope s and y-intercept b. Then we plot them against each other and do a straight line fit that describes their correlation. This straight line has two fit parameters slope m and y-intercept c. These parameters can already be used to do a pressure correction independently of the gas composition. The correction would work in this way:

If we have the gain at a given pressure $g(p_{ref}) = g_{ref}$ we know that the pressure dependence can be estimated as straight line (through the point (p_{ref}/g_{ref}). So:

$$g(p) = s \cdot p + b \tag{5.1}$$

while s is the slope an b is the y-intercept but we do not know these parameters yet. Anyway it is possible to simply calculate them with our result of 5.13 because the straight line (red dashed line in fig. 5.13) gives us the dependence of the two parameters

y-intercept b and slope s:

$$b(s) = m \cdot s + c \tag{5.2}$$

$$g = s \cdot p + m \cdot s + c \tag{5.3}$$

$$g = s \cdot (p + m) + c \tag{5.4}$$

$$s = \frac{g - c}{p + m} \tag{5.5}$$

$$b = g - s \cdot p = g - \frac{g - c}{p + m} \cdot p \tag{5.6}$$

We can insert $p = p_{ref}$ and $g = g_{ref}$.

Now it is possible to chose a reference pressure value and calculate the gain of each pad at this pressure. Then at a different pressure p_1 we can simply do the correction by multiplication of the gain with $\frac{g(p_{ref})}{g(p_1)}$ and one can calculate $g(p_1)$ with formula 5.1. The unknown parameters s and b can be derived from 5.5 and 5.6.

The above described procedure is not optimal for various reasons: The effect that the y-intercept b goes linear with the slope s seems to be only a geometrical effect because our pressure range (950 mbar - 980 mbar) is quite far away from the origin so that a shift of the gain doesn't play a role compared to a change of the slope. The slope is hence strongly correlated with the y-intercept. Furthermore the gas compostions strongly influence the parameter c but this parameter is important if we want to calculate s in 5.5. These are the reasons why it is not optimal to do a pressure correction in this way.

Thus we will now try an exponential fit as described in section 5.7.

5.7 Exponential fit

If we want to find the pressure dependency of the gain it makes sense to first exclude the influence of the gas composition. That's the reason why we look at fig. 5.10 again and now chose only two ranges C and D so that the gas composition doesn't change a lot, especially the Xe and N_2 composition that are assumed to have a large influence. These two ranges are shown with dashed black lines in fig. 5.10. Like we did it for the linear fits, graphs of gain vs pressure are made for each detector, category and range so that an exponential fit of the type: $g(p) = A \cdot exp(Bp)$ can be done. First of all we did the fits with free parameters A and B for each fit but in fact like it was discussed in the model chapter 4.2 it makes sense to assume a constant parameter B at least for each chamber and gas composition. Theoretically the slope B shouldn't change for different categories and detectors but it may depend on the gas composition because this wasn't considered in the model. In order to verify whether it is valid to assume that B is constant and how it depends on the gas composition we now look at the result of the "free" fit. In figure 5.14 one can see the variation of the parameter B for the two gas compostions.
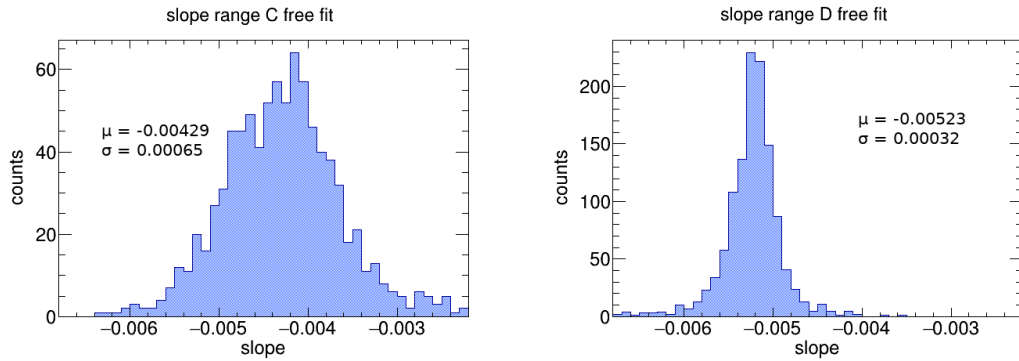
Figure 5.14: The variation of the slope for the free exponential fits in gas composition range C (left) and range D (right). We recognize that the distributions are shifted and for range C the width is bigger.

It is remarkable that the mean slope changes with gas composition and even for one range the variation of the slope is not small. Moreover range D has a smaller distribution maybe due to the fact that more data points are included.

Because we want to check whether a fixed parameter B is a good description a simultaneous fit for each detector was done. This means that for the five categories of one detector five fits are done but the parameter B must be the same and only A can vary between the categories. One can see the result in fig. 5.15.
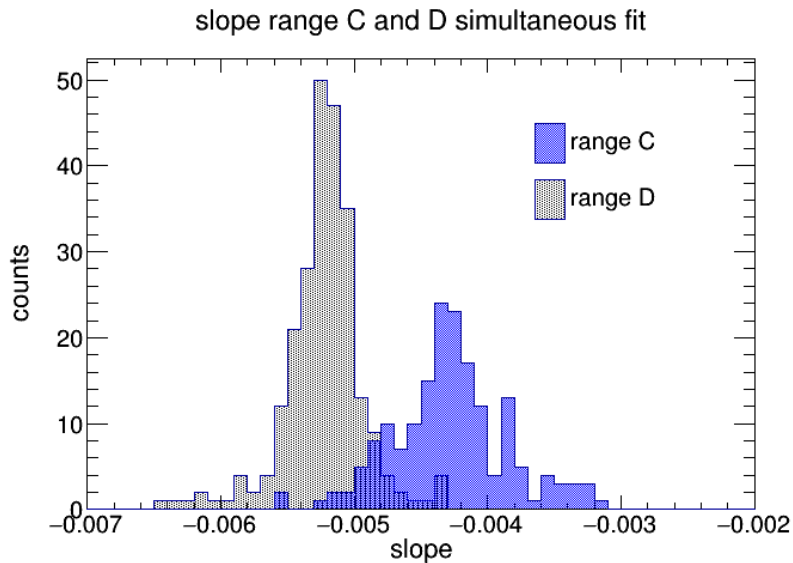
Figure 5.15: After the simultaneous fit we get the slope B of the exponentials that is plotted here for the two ranges. The shift of the distributions due to the different gas compostions is clearly visible.

One can see clearly that the gas composition influences the slope because the mean of

the distributions are shifted. Compared to fig. 5.14 the distributions look quite similar. This justifies the assumption of a fixed B for each detector. Later and in fig. 5.17 we will discuss the quality of the fit by looking at χ^2/NDF.

Actually now it has to be checked if a fixed slope for each gas compostion is still a good description. Therefore we look at the mean of the histograms for each range: $s_{rangeC} = -0.00431 \pm 0.00065$ and $s_{rangeD} = -0.00521 \pm 0.00033$.

Then an exponential fit with fixed slope for each gas composition range is done. In order to see whether this worked we look at the fits and furthermore calculate χ^2/ndf for the free fit, simultaneous fit, fit with fixed slope for each gas compostion and fit with completely fixed B. This one can see in figure 5.17.

Unfortunately we know that the gas composition influences the slope but can not exactly describe in what way it does. In order to study the behaviour we would need more data like for example a Krypton run with systematically changed gas compositions or alternatively we could use collision data but have to do a pressure and HV-correction in order to study the gas composition dependence. This is out of scope for this thesis and because data like a Krypton run for gas compositions are not available the gas composition can not be used as a parameter in our calibration so we can not find out how the slope changes with the gas composition. Furthermore the gas composition is quite complex because lots of gases play a role - see fig. 5.10 and only xenon and N_2 are considered here.

In order to find a pragmatic solution now it is checked whether a fixed slope can be used even if the gas composition changes. Therefore the mean $s_{mean} = -0.00483 \pm 0.00066$ of the slopes in krypton run is used to do a fit for all detectors and categories.

Before discussing the quality of the fits it is necessary to think about errors: The data points in the graphs gain vs pressure come from gaussian fits, so their statistical uncertainity is the error of the fit parameter μ that is quite small as one can see for example in fig. 5.3. Due to the large data size it is therefore negligible compared to a systematic error that has to be determined. As discussed earlier, the main systematics is most likely coming from the fact that many pads with slightly different gains are summed up. The mean and maximum is therefore not identical anymore. This is used to estimate a systematic error by calculating the relative difference of the maximum bin to the mean of the Gaussian. In fig. 5.16 one can see the distribution of this relative error. The relative rms of the curve is 1.2% and this is used as systematic error in the following. Because the systematic error is bigger than the statistical one it is not completely correct to talk about χ^2 but anyway it can be used to discuss the quality of the fit.

Now it has to be decided whether it is allowed to fix B by looking at χ^2/ndf in comparison to the other fits. As one can see in fig. 5.17, χ^2/ndf doesn't differ significantly regarding different fits. This can also be seen by the mean that is plotted on the left side. First of all it is suprising that the lowest mean is given by the fit with fixed B for ranges but this can be explained by the fact that there is only one parameter left so ndf = $N_{points} - N_{params}$ can become bigger. Examples for all four kinds of fits are shown in fig. 5.18. As one can see all of them are a good description for the data. In general the conclusion is that it is possible to use a fit with completely fixed B because

the quality of the fit is still good as shown by the χ^2/ndf values and the mean of it compared especially to the free fit.
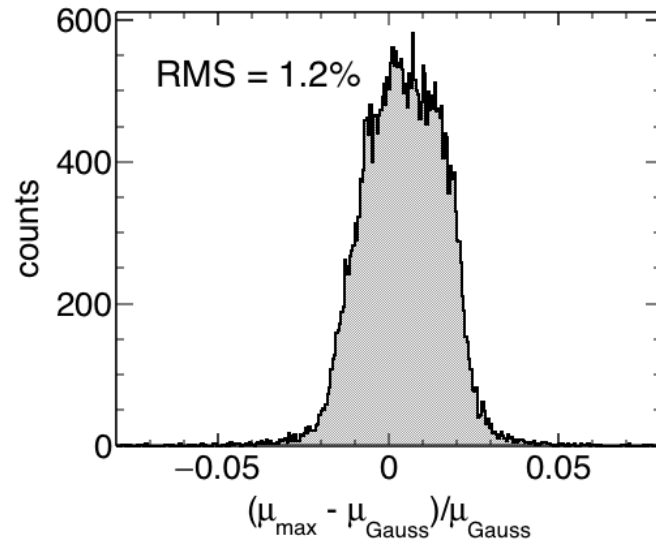

Figure 5.16: The distribution of the relative systematic error in a histogramm. The standard deviation of 1.2% is used as systematic error in the following.
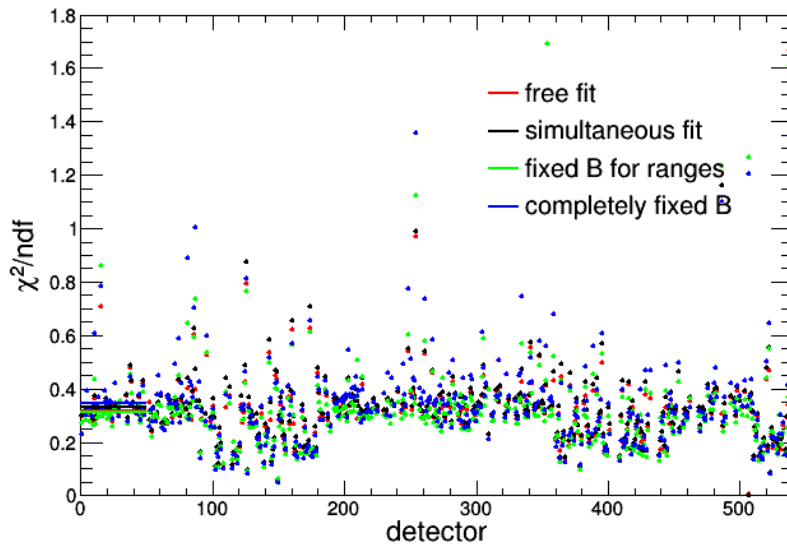

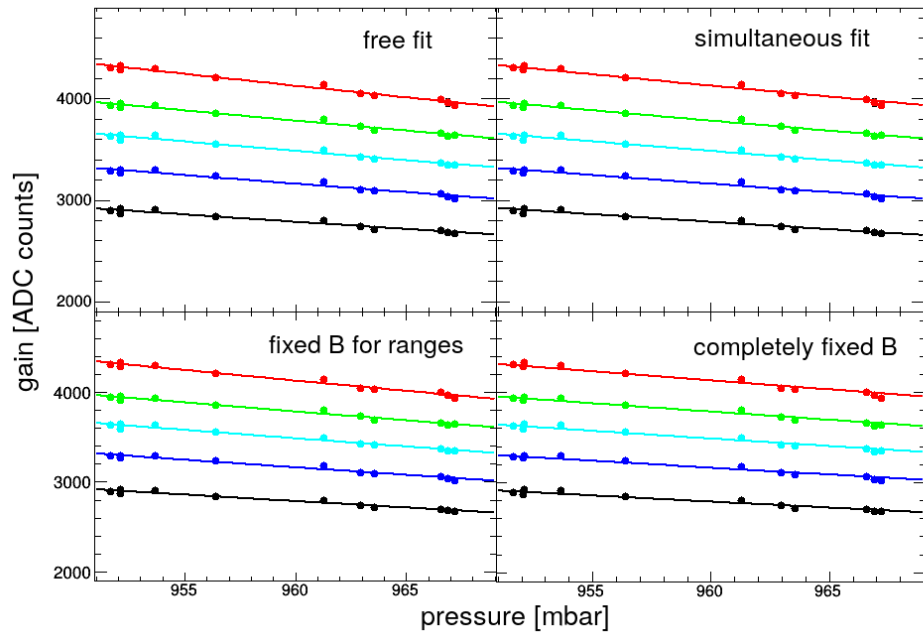Figure 5.17: χ^2/ndf is plotted for 4 kinds of fits. Furthermore the left stripes show the mean for each fit.

Figure 5.18: Four kinds of fits for detector 11.

5.8 Pressure correction of the gain

Because it is possible to describe the pressure dependence by an exponential function with only one free parameter A, a pressure correction can be done in the following way:

With a pad and its gain g_{ref} at a pressure value p_{ref} which is given by the Krypton calibration, one can calculate the curve that describes the pressure dependence of this pad.

$$g(p) = A \cdot exp(Bp) \tag{5.7}$$

$$g_{ref} = A_{ref} \cdot exp(-0.00483 \cdot p_{ref}) \tag{5.8}$$

$$A_{ref} = \frac{g_{ref}}{exp(-0.00483 \cdot p_{ref})}) \tag{5.9}$$

And now one can easily correct a measured gain g_{measured} at a pressure p_1 to the gain at a reference pressure p_{ref}:

$$g_{\text{corrected}} = g_{\text{measured}} \cdot \frac{g(p_{ref})}{g(p_1)} \tag{5.10}$$

So it is possible to eliminate the pressure dependence by calculation. Anyway the gains still vary because of geometrical reasons as described by the categories and furthermore it depends on the high voltage. The next chapter will be about this dependency.

6 High voltage calibration

In the previous chapter the pressure dependence of the gain is considered and as a result we got an exponential dependence of gain with pressure. Furthermore we found that the slope of these exponentials can be estimated as constant. Due to these results it is possible to do a pressure correction.

In the following we want to study the high voltage (HV) dependence of the gain.

6.1 Gain vs high voltage

In general we did it analogously to the pressure dependence: We used the same categories and instead of different pressure values we used the ADC spectra which were taken during the high voltage scan. Fortunately the pressure during the HV scan was approximately constant so that a pressure correction of the data has not to be done. The procedure of the HV scan for one detector can be seen in fig. 6.1. There are seven different HV settings each with one, two or four runs. The high voltage varied in a range from $-15\,\mathrm{V}$ up to $30\,\mathrm{V}$ around the nominal setting.

Again we summed up the spectra for each category, did Gaussian fits, got the pulse height of the main krypton peak and plotted it against the high voltage value. In some cases the ADC krypton spectrum was biased because of single pads that fired continuously. Thus we had to find theses spectra by looking at the number of entries and sort them out. One can see the result for some example detectors in fig. 6.2.
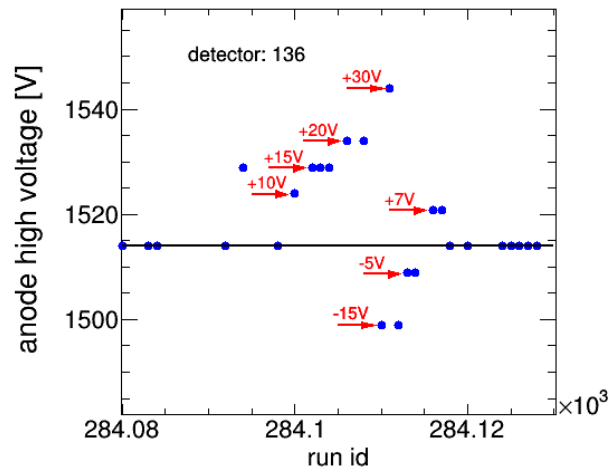
Figure 6.1: Procedure of the HV scan for one example detector. The black line shows the normal HV setting and the arrows demonstrate how the high voltage was varied.
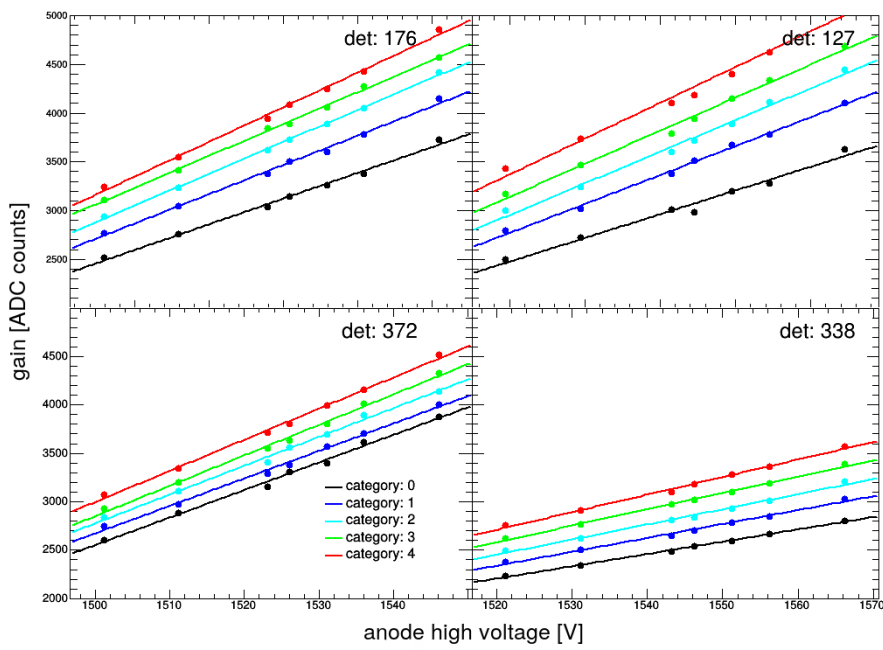

Figure 6.2: The gain increases linearly with high voltage. One can see that the slopes change with the gain category.

36

The gain increases approximately linearly with higher voltage. Thus linear fits were done in fig. 6.2 and now we know how the high voltage setting influences the gain for each detector and category. One can describe the gain as a function of high voltage: $g(HV) = s_{HV} \cdot HV + y_{HV}$ while s_{HV} and y_{HV} depend on the detector and the category. In section 6.2 it is described how the high voltage can be used to do a pressure correction directly. In section 6.3 we try to find the optimal HV settings so that the gain variations are minimized.

6.2 Pressure correction by HV adjustment

As mentioned above a pressure correction by adjusting the high voltage will be reviewed.

6.2.1 Example calculation

First of all an example calculation is done. For a single pad it is possible to correct the pressure change by an HV adjustment:

If the gain at the reference pressure p_1 is known and the pressure is changed to p_2 there is a change in gain Δg. By the approximation $g(p) = A \cdot exp(Bp)$ one can calculate $\Delta g = A \cdot exp(Bp_2) - A \cdot exp(Bp_1)$.

In order to compensate it by a HV change:

$$\Delta g = -\Delta g_{HV} \tag{6.1}$$

$$A \cdot (exp(Bp_2) - exp(Bp_1)) = -s_{HV} \cdot (HV_2 - HV_1) \tag{6.2}$$

$$HV_2 = -\frac{A}{s_{HV}} \cdot (exp(Bp_2) - exp(Bp_1)) + HV_1 \tag{6.3}$$

However a high voltage correction is only possible for a whole TRD detector module and not for single pads. Due to that we have to examine if the high voltage change is the same for every pad. That's in general not the case because A and s_{HV} depend on the gain of the pad or in other words on the category. But it might be possible that $\frac{A}{s_{HV}}$ is constant. In order to check this I first look at one detector for example at detector 176 - see fig. 6.2. If you choose category 0 (black line) at $HV_1 = 1500$ V then its gain is 2835 ADC counts. During the HV scan the pressure was at p = 968.7 mbar so one can calculate A_{cat0}: $A_{\text{cat0}} = 2835/exp(pB) = 3.733 \cdot 10^5$. Analogously it can be done for category 4 (red line) also at 1500V: g=3719 ADC counts and $A_{\text{cat4}} = 3719/exp(pB) = 4.897 \cdot 10^5$. The slopes of the HV curve are known from our fit: $s_{\text{HVcat0}} = 26.42$ and $s_{\text{HVcat4}} = 35.58$. So now one can calculate $\frac{A}{s_{HV}}$ for both pads and check whether they are approximately the same.

$$\frac{A_{\text{cat0}}}{s_{\text{HVcat0}}} = 14129 \tag{6.4}$$

$$\frac{A_{\text{cat4}}}{s_{\text{HVcat4}}} = 13762 \tag{6.5}$$

Apparently they are nearly the same because the deviation is only around 3%. So fortunately if one goes from category 0 to 4, the positive slope change in the HV seems

to compensate the change of parameter A. Of course this is not sufficient to prove that a pressure correction can be done in that way because it is only an example. Thus we want to try a pressure correction by high voltage now for all pads (represented by categories) of one detector and after that for all detectors. Therefore we look at the gain distributions.

6.2.2 Correction for all detectors

First one detector e.g. 11 is chosen and gain vs pressure like in fig. 5.9 is used to get Δgain$=\Delta g$ for each category due to a pressure change. As an example a pressure change from p_1=953.6 mbar to p_2=963.6 mbar is applied and in this case the gain change wasn't calculated by the formula because you can simply use the measured data. Then one have to calculate a ΔHV that will correct Δg and this can be done with formula 6.1 if you use as Δg the one from category 2 for example and apply the s_{HV} for each category we get from fig. 6.2. Then the gain after the correction by the HV adjustment can be calculated and compared to the gain before the pressure change. This is shown in fig. 6.3. If one changes the pressure then the gain changes for each category from the black to the blue value. After that the HV correction is done and the calculated gain is shown by the red circles. One can see that the deviation is so small that the positions of the red markers is nearly indistinguishable of those from the black ones so the HV correction is really precise.

Of course this was only one example detector so the same has to be done for each other detector and category. In order to check the quality of the correction one can calculate the ratio $g_{p1}/g_{HVcorrected}$ for each detector and category. Then the mean of it (summed up and divided by 5) is a quality criterium for the correction. Before doing that we had to sort out the detectors that don't work. In fig. 6.4 the mean ratio for each detector is plotted against the detector number and as expected it is very close to one except for three outliers. That shows that a pressure correction by HV adjustment is possible with this new method.
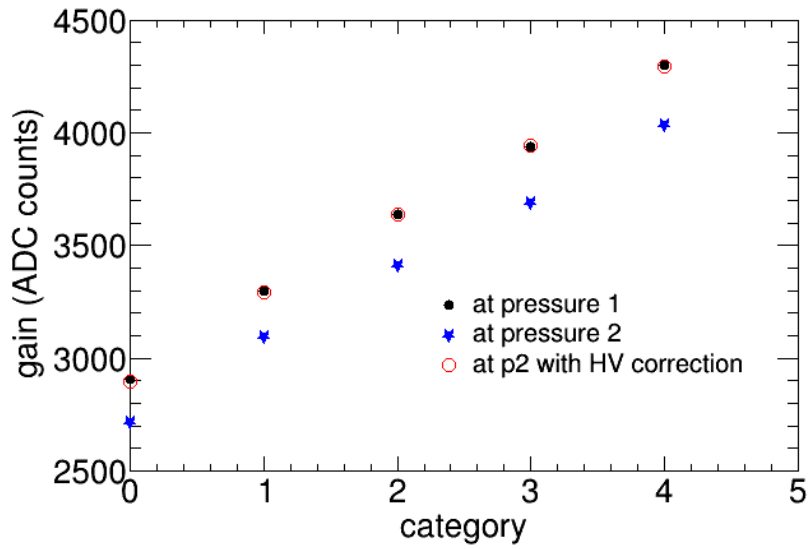
Figure 6.3: For detector 11 one can see the gain at an initial pressure p_1=953.6 mbar (black dots) and after a pressure change to p_2=963.6 mbar. Then we calculate a HV adjustment so that the pressure is corrected and calculate the resulting gain (red circles).
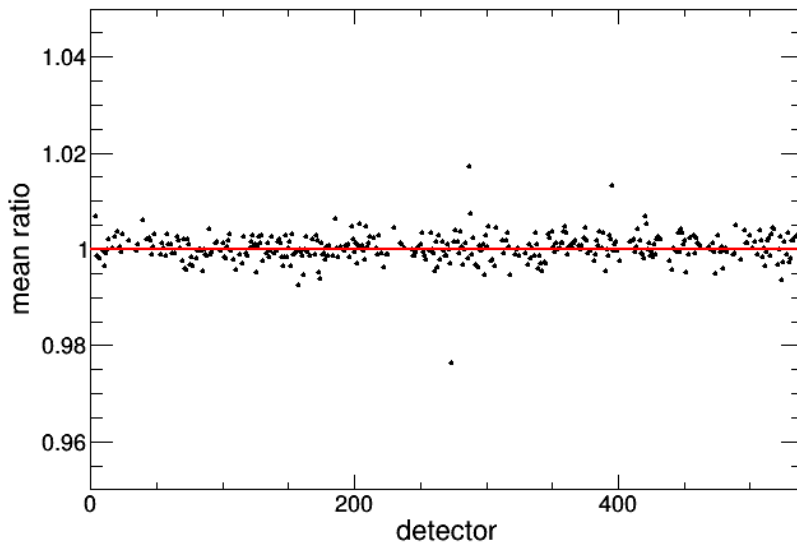

Figure 6.4: For every detector we sum up the ratio of the gains at an inital pressure divided by the gains after pressure correction for each category and calculate the mean of it.

6.3 HV adjustment for each chamber

As described before one can correct the gain changes caused by changes in the ambient pressure by a HV adjustment. Furthermore it is possible to find an optimal high voltage setting, so that each chamber nearly has the same gain. Due to the fact that the gains within a chamber vary and one can only adjust the HV for each detector it is impossible to calibrate every detector exactly to the same gain (at one pressure). In fact we have to look at the deviations of the pads from the desired gain and minimize it by varying the HV. We used a desired gain of 3100 ADC counts and summed up the deviations Δg_i for each category i:

$$\Delta G = \sqrt{\sum_{i=0}^{5} |\Delta g_i|^2} \tag{6.6}$$

Δg_i is the deviation of category i from the desired gain at a chosen high voltage. So the minimum of ΔG gives us the optimal HV for each chamber. We did that for each detector and the optimal high voltage as well as the change of the HV is plotted in fig. 6.6

In order to see how much the gain variance was improved one considers $\Delta G/G$ for each detector as shown in fig. 6.5 (middle part) and calculates the mean of it (dashed line). In order to compare it with the unadjusted HV therefore also the gain deviations have to be calculated but in this case one has to think about which reference gain to take. It makes sense to calculate the deviations from the mean gain of the whole TRD, that first has to be calculated. This mean gain is 3371 ADC and now ΔG is calculated for the unadjusted HV as shown in fig. 6.5 (upper part). If one compares the two plots the mean gain deviation as well as the rms was decreased by adjusting the HV, so the adjustment was successful. Moreover the ratio (lower part) is usually smaller than 1 what means that for each detector the adjustment lowered ΔG. As one can see by the mean of the ratio that is about 0.9 the optimization is in the order of 10 %.

Furthermore we want to think about the optimal reference gain, because 3100 ADC counts was chosen randomly. Therefore the procedure above was repeated for different reference gains and the minimum of mean gain deviation and rms was calculated. The result is shown in fig. 6.7. As one can see, there is a minimum in each plot but in fact it does not really matter because the differences are quite small. Thus a desired gain of 3371 ADC was chosen which is identical to the mean gain before adjustment. Then the steps described above were repeated and again one gets as result the optimal HV setting as shown in fig. 8.7a and the HV change compared to the former HV setting fig. 8.7b as well as delta gain for each detector fig. 8.9. So the calculated optimal high voltages were implemented for the 2018 run and are currently in use.
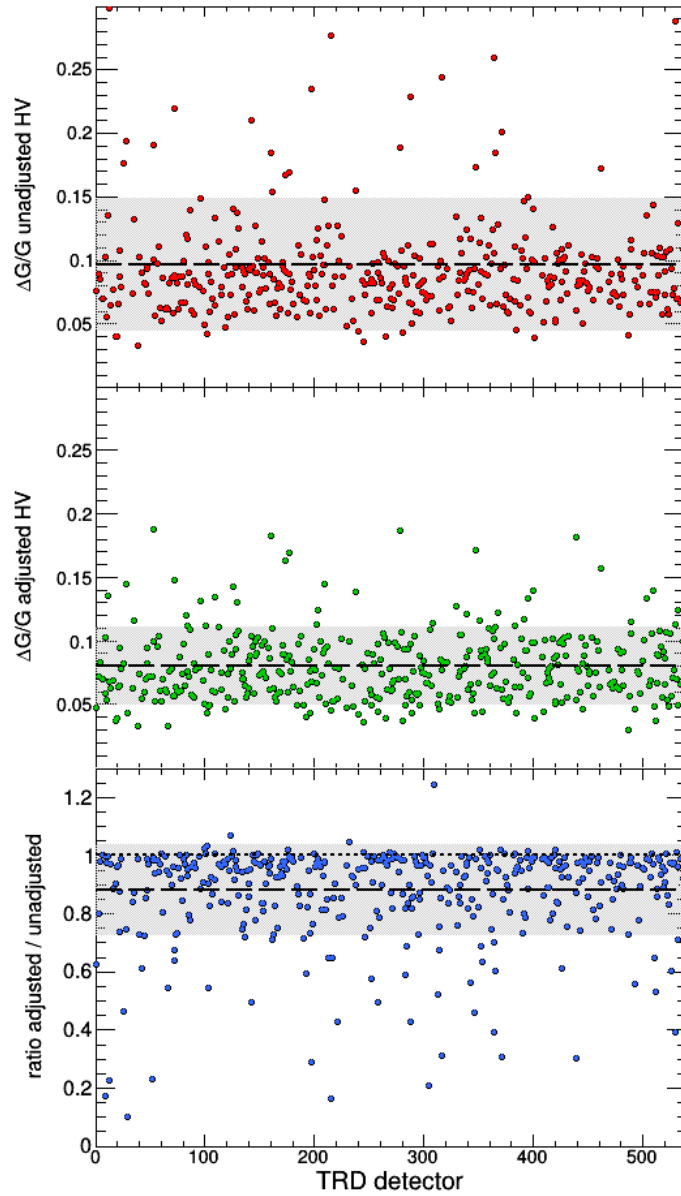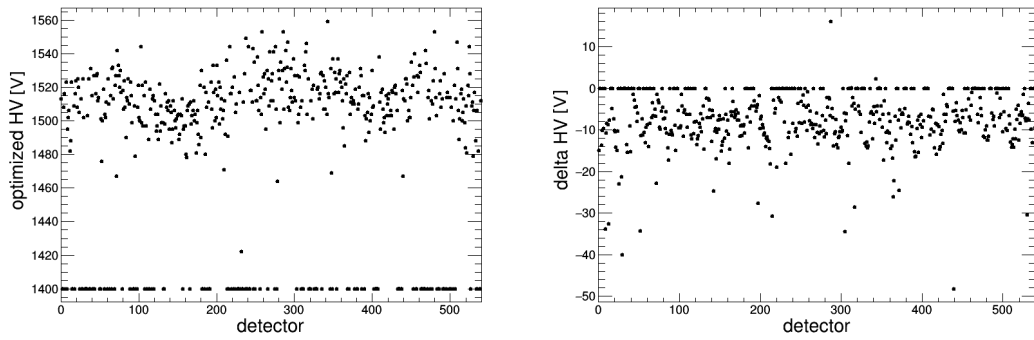
Figure 6.5: Top: Relative gain deviations from the mean gain with unadjusted HV. The grey shaded region is the rms. Middle: Relative gain deviations from our desired gain of 3100 ADC counts but with our calculated and adjusted HV. The mean and the the rms is lower than in the upper part. Bottom: The ratio of middle over top.

(a) Optimized HV to achieve a mean gain of (b) Relative voltage adjustment to get the
    3100 ADC counts. The value for detectors   optimal gains. Because 3100 ADC counts
    which do not work is set to 1400V.   as desired gain is quite low nearly all HVs
                                    have to be lowered in order to achieve this
                                    gain.

Figure 6.6
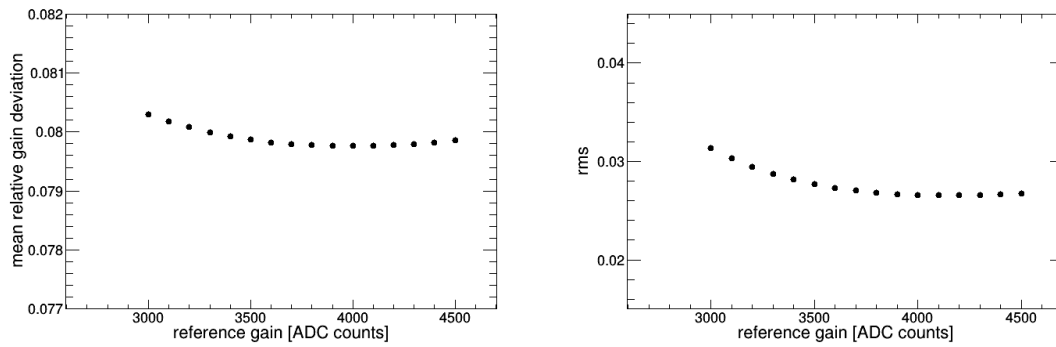
(a) Mean gain deviation plotted against the (b) The rms is plotted against the reference
    reference gain. There is a minimum but the   gain we choose.
    change is quite small.
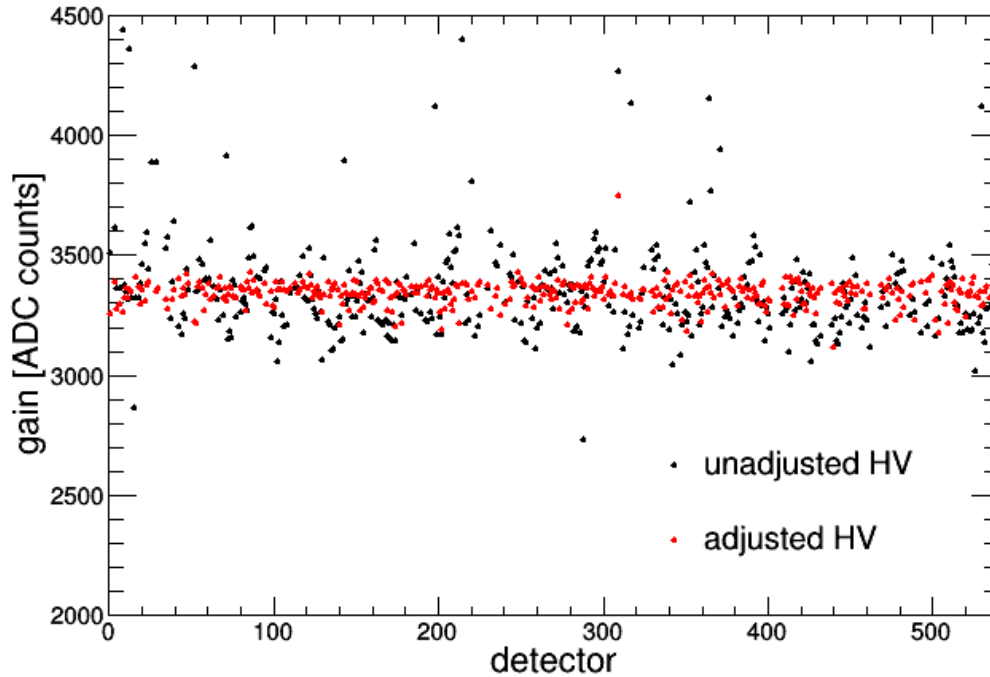
Figure 6.7

Figure 6.8: Gains of category 2 for each detector without and with adjusted HV at pressure p=986.7 mbar.

In fig. 6.8 there are the gains of category 2 for each detector. For the unadjusted high voltages the gains are shifted to the pressure p=986.7 mbar during the HV run so that they are comparable to those with adjusted HV. The gains with adjusted HV are calculated by the straight line fits shown in fig. 6.2 using the optimal HV settings - see fig. 8.7a.

As one can see in fig. 6.8, before the HV adjustment there was a Θ-structure probably due to a not working path length correction. One have to consider the full trajectory of a particle crossing the detector. So for each stack there is a different path length due to the angle Θ and thus the charge deposited in the detectors depends on Θ. Because each supermodule consists of 6 layers and 5 stacks there is a repetition of the structure after 30 detectors - see also fig. 8.8 The adjustment of the HV leads to a significant improvement of the gain deviations as shown by the decreased spread of the red dots. So by minimizing the gain deviations by adjusting the high voltage settings it is possible to effectively correct for the Θ-structure. Moreover the exponential behaviour of the gain with pressure - described in section 5.7 can be used to calculate the gain change with pressure and it can be corrected by an HV adjustment as explained in section 6.2.

7 Summary

First a model was developed that is qualitatively able to calculate the final number of electrons per traversing particle inside the TRD (that is proportional to the gain) and explain the inverse pressure dependence of the gain due to the first Townsend coefficient. Moreover for the simulated data linear and exponential fits were made to describe the pressure dependence. As a result we got that an exponential fit with fixed slope is the best description.

Then krypton data are used to study the pressure dependence. We divided all detector modules in gain categories because pads with different gains depend on pressure in a different way. For these categories we summed up the kryton spectra and did Gaussian fits in order to get data of gains at various pressures. After that linear and exponential fits were done. Both fits are possible but in fact it is an advantage to use exponential fits because on the one hand they fit to the model and on the other hand we can use only one fit parameter as discussed later. As we showed the gas composition has an influence on the gain and furthermore on the slope of the exponentials but anyway it is possible to use a fixed slope with acceptable precision so that only one parameter is left that can be calculated easily. With that in hand a calibration can be done.

Furthermore the high voltage dependence of the gain was studied. The increase of the gain with high voltage is approximated by straight line fits. Then it is shown that a pressure correction can be done by a high voltage adjustment. Moreover with the former HV settings the gains of the detectors differ and a Θ-structure is visible. By calculating optimal high voltage settings it is possible to minimize the gain deviations and correct the Θ-structure. So we can achieve a significant improvement in run 3 by adjusting the HV in order to decrease gain deviations and furthermore correct the pressure dependence of the gain by changing the high voltage. With that method the HV settings were already improved for the year 2018 data taking.

8 Appendix

Because actually some plots weren't shown in the main part of the Bachelor Thesis they will be presented here.
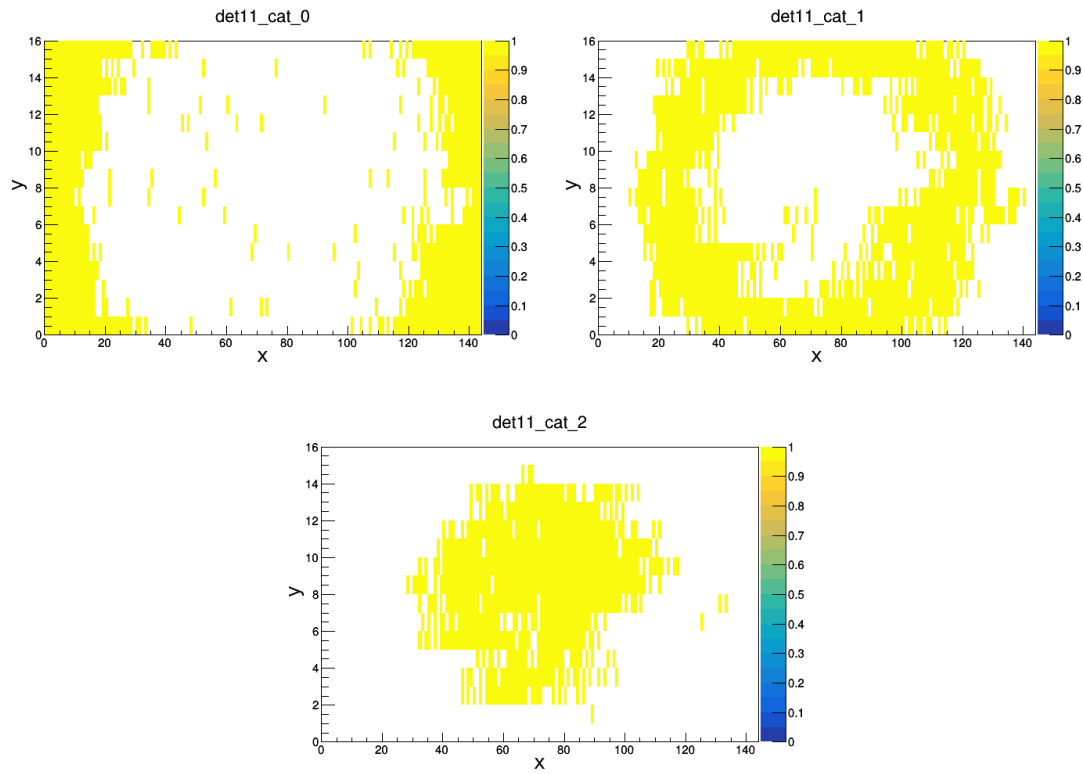

Figure 8.1: The division of detector 11 in 3 categories. Obviously the pads with different gains are not randomly distributed but geometrically together.
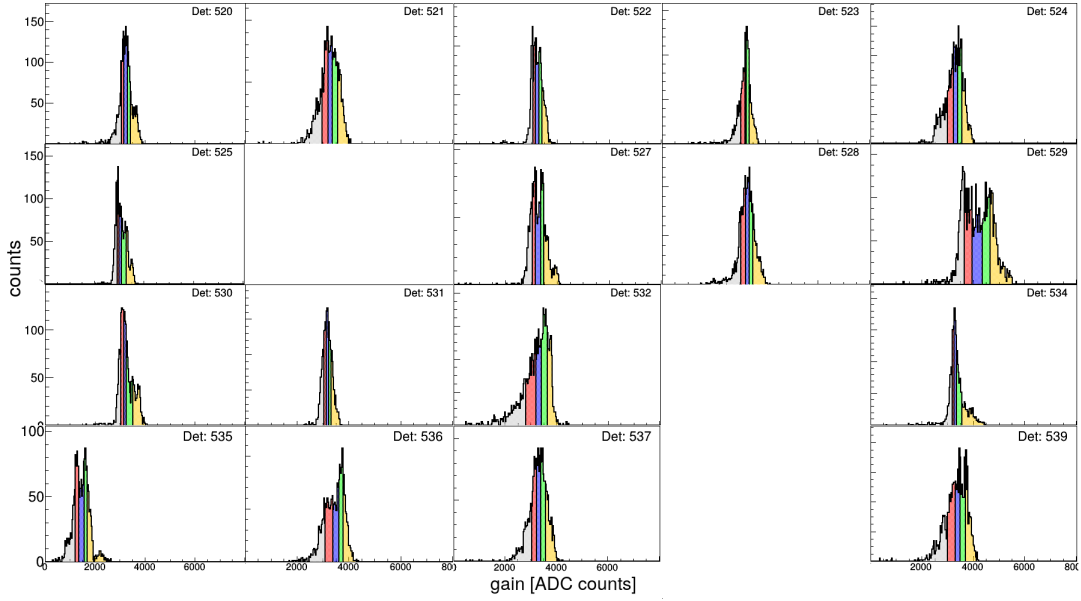
Figure 8.2: The division of the gain distributions in categories like in fig. 5.7.
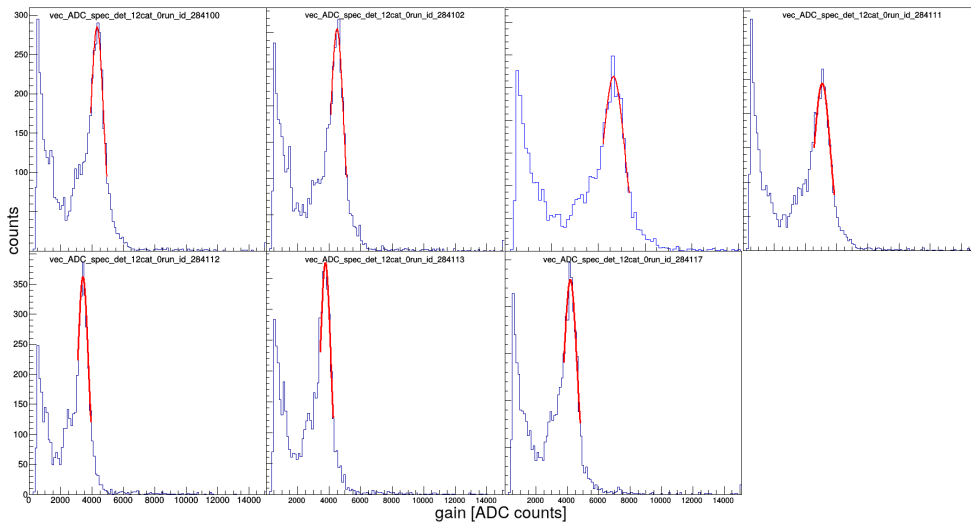

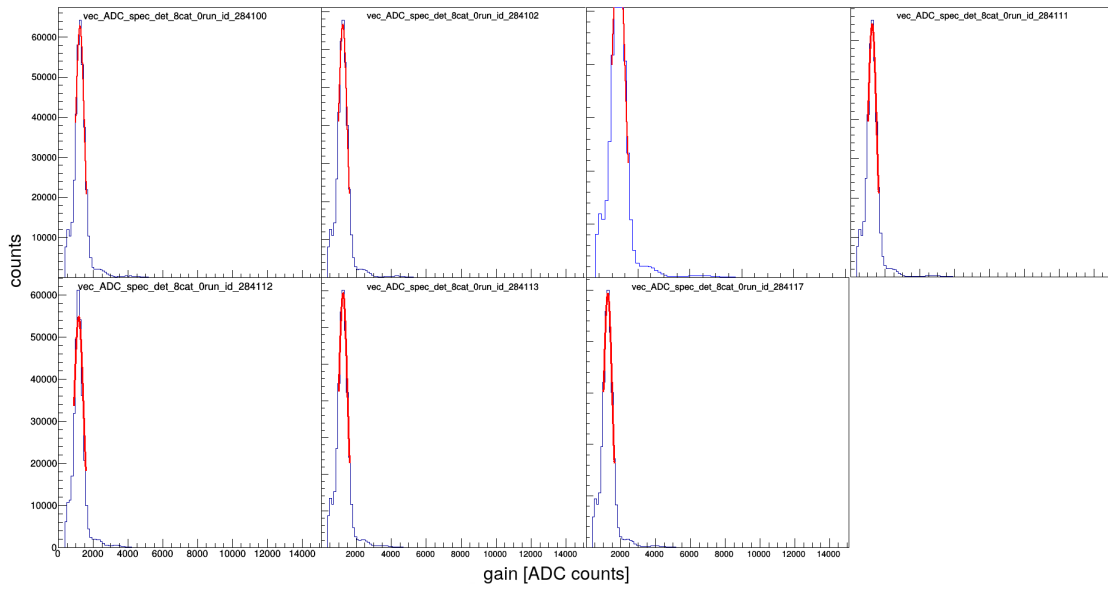Figure 8.3: Krypton spectra of detector 12 and category 0 for different run ids. In red there is the Gaussian fit for the main krypton peak.

Figure 8.4: In detector 8 and category 0 there is at least one defect pad that fires continously what can be seen by the high number of counts. Thus this spectrum had to be sorted out.
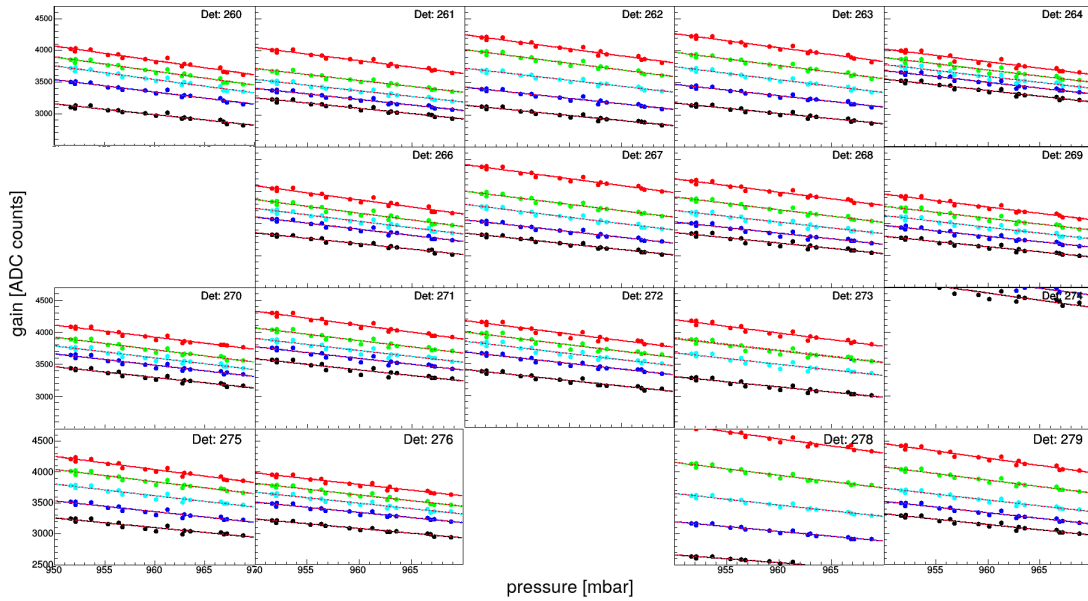
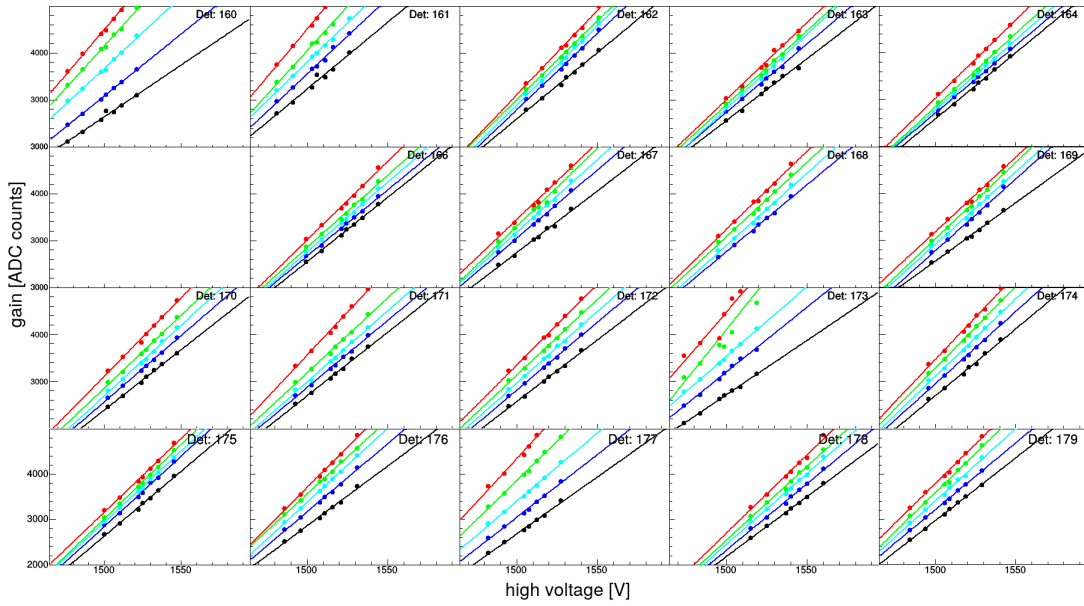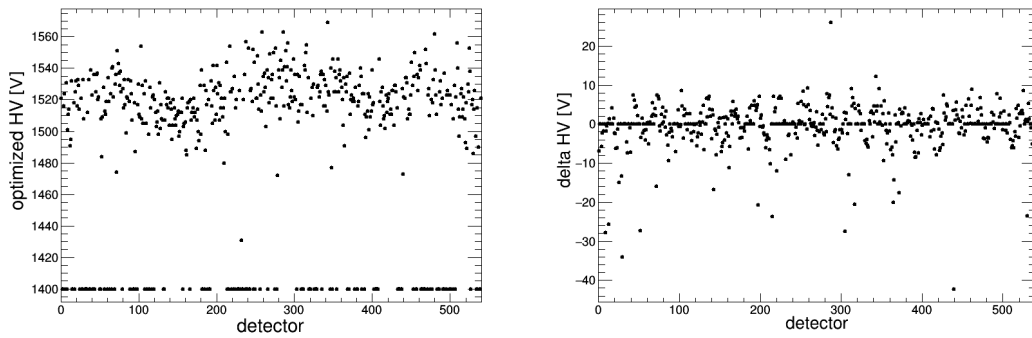Figure 8.5: Gain vs. pressure like in fig. 5.9 but for more example detectors.

Figure 8.6: The gain increases linearly with high voltage as already shown in fig. 6.2. One can see gain vs HV here for more example detectors with straight line fits.

(a) It is the same plot as 6.6a but with 3371 as reference gain.

(b) Delta HV is plotted. In comparison to 6.6b now the HVs for some detectors have to be increased.
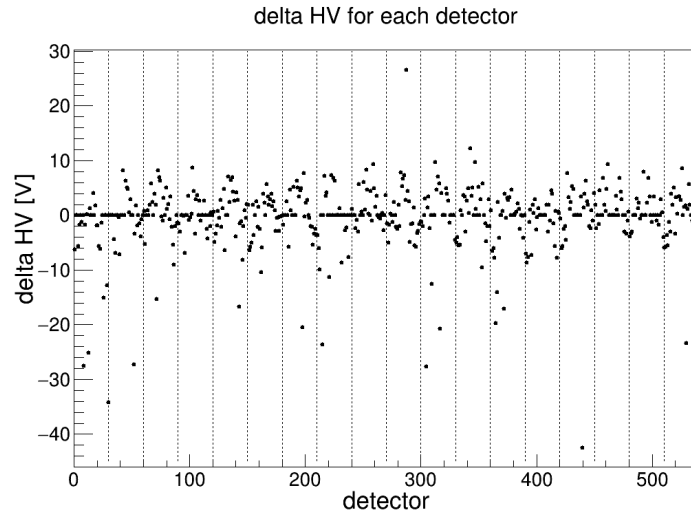
Figure 8.7

Figure 8.8: If we look closer at fig. 8.7b then we can see a structure for each supermodule (shown by the vertical lines).
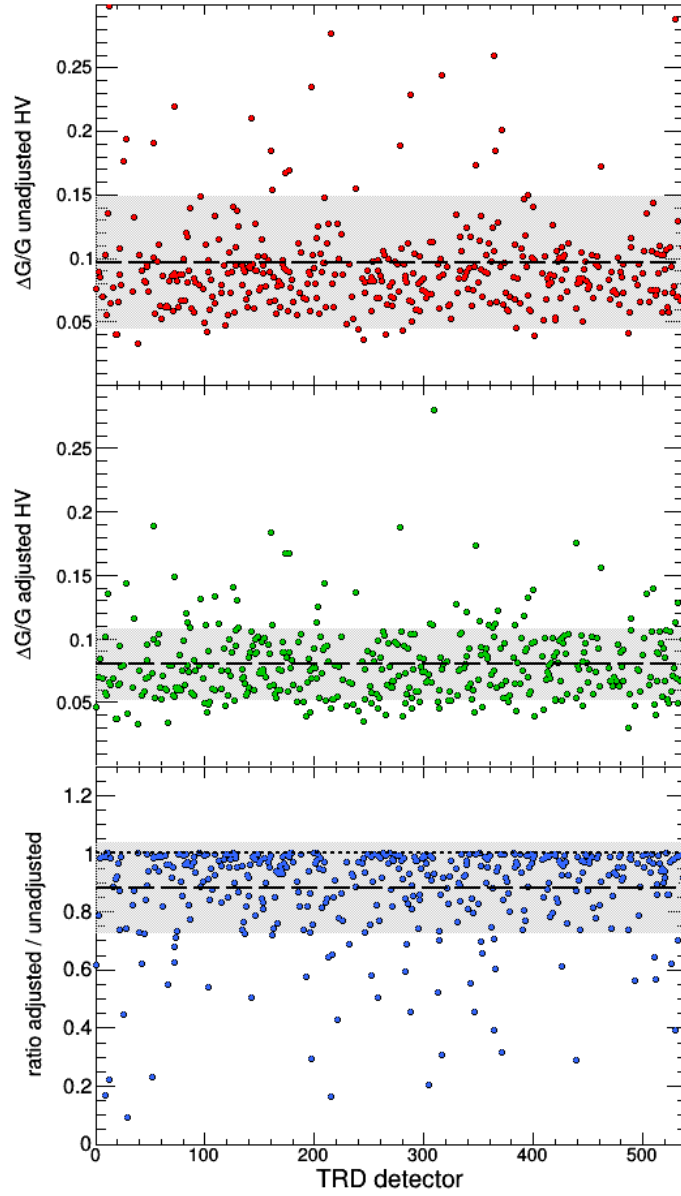
Figure 8.9: In general this is the same figure as fig. 6.5 but with 3371 ADC counts as reference gain that is the actual mean gain of all detectors. We see again the decreasement of mean ΔG/G and rms. An improvement of $\propto 10\%$ can be estimated.
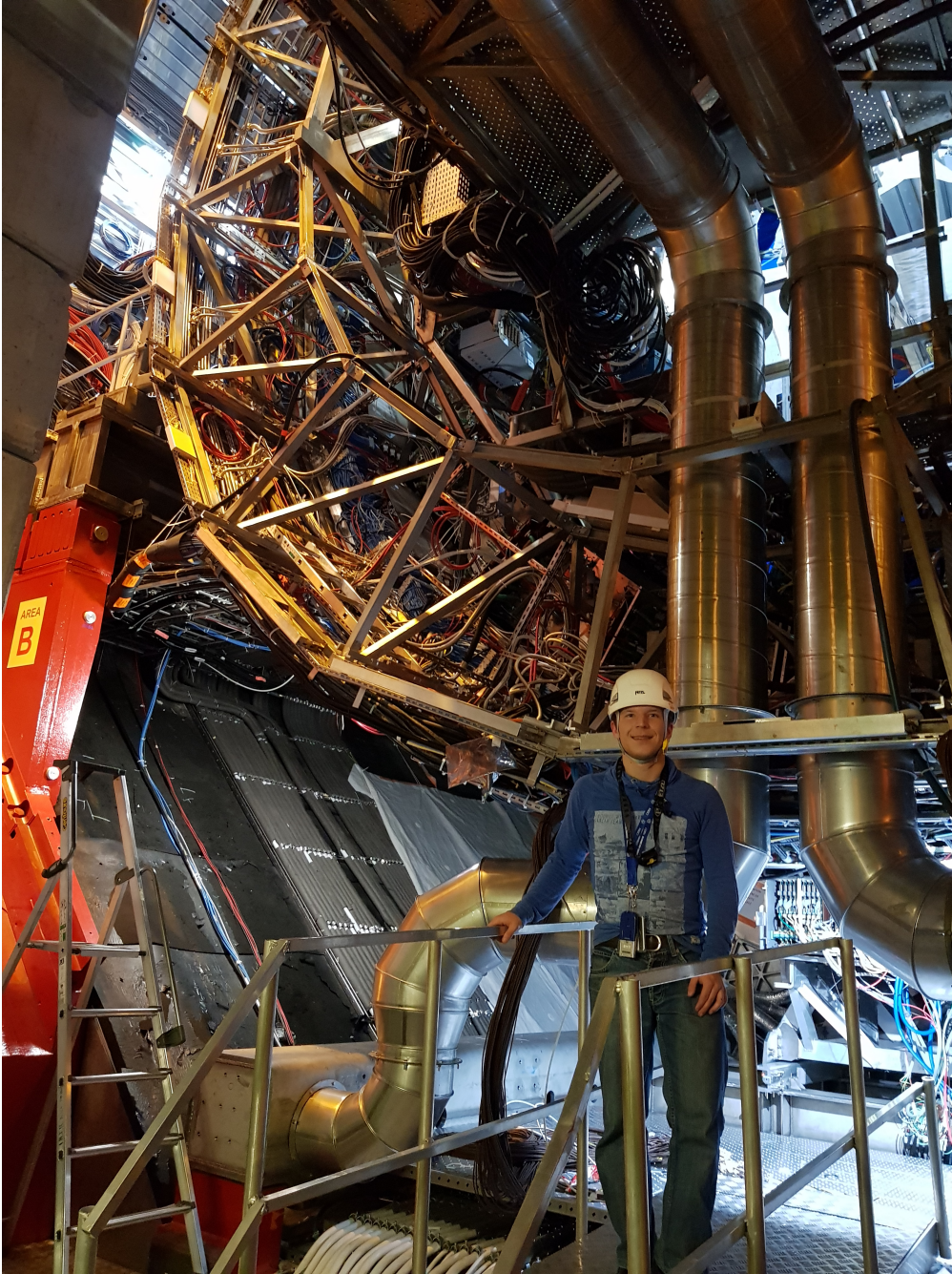
Figure 8.10: Me in front of the ALICE detectors.

Figure 8.11: The TRD supermodule 6 was removed after we had uncabled it.

Acknowledgements

Bibliography

[1] M. Gell-Mann, "Progress in elementary particle theory, 1950 - 1964", CALT-68-1426 DOE Research and Development Report, url: `https://www.researchgate.net/publication/300442501_Progress_in_elementary_particle_theory_1950-1964`.

[2] A. Chodos, R. L. Jaffe, K. Johnson, C. B. Thorn and V. F. Weisskopf, "A New Extended Model of Hadrons," Phys. Rev. D **9** (1974) 3471. doi:10.1103/PhysRevD.9.3471.

[3] O. F. Akinto and F. Tahir, "Strong Gravity Approach to QCD and General Relativity," arXiv:1606.06963 [physics.gen-ph].

[4] Lucia Leardini, "Measurement of neutral mesons and direct photons in Pb–Pb collisions $\sqrt{s} = 2.76$ TeV with the ALICE experiment at the LHC.", page 6, Ph.D thesis, University of Heidelberg, unpublished (2017).

[5] D. J. Gross and F. Wilczek, "Asymptotically Free Gauge Theories - I," Phys. Rev. D **8** (1973) 3633. doi:10.1103/PhysRevD.8.3633.

[6] J. D. Bjorken, "Highly Relativistic Nucleus-Nucleus Collisions: The Central Rapidity Region," Phys. Rev. D **27** (1983) 140. doi:10.1103/PhysRevD.27.140

[7] A. Andronic, P. Braun-Munzinger, K. Redlich and J. Stachel, "Decoding the phase structure of QCD via particle production at high energy," Nature **561** (2018) no.7723, 321 doi:10.1038/s41586-018-0491-6 [arXiv:1710.09425 [nucl-th]].

[8] E. Abbas *et al.* [ALICE Collaboration], Phys. Rev. Lett. **111** (2013) 162301 doi:10.1103/PhysRevLett.111.162301 [arXiv:1303.5880 [nucl-ex]].

[9] M. A. Winn, "Inclusive J/ψ production at mid-rapidity in p-Pb collisions at $\sqrt{s_{NN}}$=5.02 TeV," CERN-THESIS-2016-031.

[10] `https://home.cern/about/who-we-are/our-history`, last checked 27.11.2018.

[11] `https://cds.cern.ch/record/2317058/files/CERN-HR-STAFF-STAT-2017-RESTR.pdf`, last checked 30.11.2018.

[12] Tim Berners-Lee, CERN, "Information Management: A Proposal", March 1989, url: `http://www.w3.org/History/1989/proposal.html`.

[13] G. Charpak, R. Bouclier, T. Bressani, J. Favier and C. Zupancic, "The Use of Multiwire Proportional Counters to Select and Localize Charged Particles," Nucl. Instrum. Meth. **62** (1968) 262. doi:10.1016/0029-554X(68)90371-6.

[14] `http://www.lhc-facts.ch/index.php?page=linac`.

[15] `http://www.lhc-facts.ch/`, last checked 27.11.2018.

[16] G. L. Ma and Z. W. Lin, "Predictions for $\sqrt{s_{NN}}$ = 5.02 TeV Pb+Pb Collisions from a Multi-Phase Transport Model," Phys. Rev. C **93** (2016) no.5, 054911 doi:10.1103/PhysRevC.93.054911 [arXiv:1601.08160 [nucl-th]].

[17] `https://lhc-machine-outreach.web.cern.ch/lhc-machine-outreach/collisions.htm`, last checked 20.12.2018.

[18] `http://www.lhc-facts.ch/index.php?page=alice`, last checked 27.11.2018.

[19] K. Aamodt *et al.* [ALICE Collaboration], JINST **3** (2008) S08002. doi:10.1088/1748-0221/3/08/S08002.

[20] Klaus Reygers, Kai Schweda, lecture "Space-time evolution of the Quark Gluon Plasma", University of Heidelberg, url: `https://www.physi.uni-heidelberg.de/~reygers/lectures/2013/qgp/qgp_ss13_06_qgp-evolution-bw.pdf`.

[21] J. Baechler [ALICE Collaboration], "The ALICE TPC," doi:10.1142/9789812773678_0002.

[22] P. Cortese [ALICE Collaboration], "ALICE transition-radiation detector : Technical Design Report," ALICE-TDR-9, CERN-LHCC-2001-021, LYCEN-2001-97.

[23] S. Acharya *et al.* [ALICE Collaboration], "The ALICE Transition Radiation Detector: construction, operation, and performance," Nucl. Instrum. Meth. A **881** (2018) 88 doi:10.1016/j.nima.2017.09.028 [arXiv:1709.02743 [physics.ins-det]].

[24] Valencia Palomo, L. (2017). "The ALICE experiment upgrades for LHC Run 3 and beyond: contributions from mexican groups." Journal of Physics: Conference Series. 912. 012023. 10.1088/1742-6596/912/1/012023.

[25] Professor Dr. Johanna Stachel, Skript "Detectors in Nuclear and Particle Physics" (2018), url: `https://www.physi.uni-heidelberg.de/~fschney/detektoren/detector_all.pdf`.

[26] Chinese Physical Society, "Chinese Physics C Volume 38 Number 9" (2014), page 399.

[27] R.F.Doolittle, U.Pollvogt, A.J.Eskovitz, "MULTIWIRE PROPORTIONAL CHAMBER DEVELOPMENT" (1973), url: `https://ntrs.nasa.gov/archive/nasa/casi.ntrs.nasa.gov/19730013483.pdf`.

[28] Y. I. Davydov, "On the first Townsend coefficient at high electric field," IEEE Trans. Nucl. Sci. **53** (2006) 2931 doi:10.1109/TNS.2006.881543 [physics/0409156 [physics.ins-det]].

[29] D. Pinci and A. Sarti, "Study of the MWPC gas gain behaviour as a function of the gas pressure and temperature," CERN-LHCB-2005-079.

[30] Luisa Bergmann, "Studies of the Gain and Drift Velocity for the ALICE Transition Radiation Detector at the CERN LHC" (2017), bachelor thesis, University of Heidelberg.

[31] Johannes Hendrik Stiller, "Gain Calibration of the ALICE TRD using the Decay of ^{83m}Kr and Alignment of the ALICE TRD", Diploma Thesis (2011), University of Heidelberg.

[32] Mustapha Al Helwi, "Gain Calibration of the ALICE Transition Radiation Detector with Krypton-83", Diploma thesis (2010), University of Heidelberg.

[33] M. Al Helwi, A. Andronic, Y. Pachmayer, N. Pitz, C. Garabatos, K. Schweda, J. Stachel, and J. Wiechula, "Gain Calibration of the ALICE TRD with Krypton (^{m83}Kr)" (2009), url: `https://pdfs.semanticscholar.org/3aab/bd0bcf034f6ed6ca43ea5b532bc4697eb62b.pdf`.

[34] Dr. A. Schmah, private communication (2018).

Erklärung

Ich versichere, dass ich diese Arbeit selbstständig verfasst und keine anderen als die angegebenen Quellen und Hilfsmittel benutzt habe.

Heidelberg, den 20.12.2018,